

## SUPPLEMENTARY INFORMATION

### **Unveiling Dual Linkages 3D Hexaiminobenzene Metal–Organic Frameworks towards Long-Lasting Advanced Reversible Zn–Air Batteries**

Sambhaji S. Shinde<sup>†</sup>, Chi Ho Lee<sup>‡</sup>, Jin-Young Jung<sup>†</sup>, Nayantara K. Wagh<sup>†</sup>, Sung-Hae Kim<sup>†</sup>,  
Dong-Hyung Kim<sup>†</sup>, Chao Lin<sup>†</sup>, Sang Uck Lee<sup>‡##</sup>, Jung-Ho Lee<sup>†\*</sup>

*<sup>†</sup>Department of Materials Science and Chemical Engineering, <sup>‡</sup>Department of Bionano  
Technology, <sup>#</sup>Department of Chemical, and Molecular Engineering, Hanyang University,  
Ansan, Kyunggido, 15588, Republic of Korea*

#### **List of Contents**

##### **1. Experimental methods**

**Catalyst Preparation**

**Catalyst Characterization**

**Oxygen Reduction Reaction Kinetics**

**Functionalized bio-cellulose membrane**

**Metal-Air Battery Performance**

##### **2. Theoretical Methods**

**Computational Details and Modeling**

**OER and ORR Reaction Pathways**

**Derivation of the Free Energy Relations**

**Free Energy Diagram (FED) and Overpotential ( $\eta$ )**

**Supplementary Figures**

**Supplementary Tables**

**Supplementary Videos**

**Supplementary References**

## **1. Experimental Methods**

### **Catalyst Preparation**

#### **Chemicals**

Chloroanilic acid ( $C_6H_2Cl_2O_4$ ), ethylenediamine ( $NH_2CH_2CH_2NH_2$ ), 1-methyl-2-pyrrolidinone ( $C_5H_9NO$ ), manganese(II) nitrate, TX-100, and iron(II) oxide were obtained with the Sigma-Aldrich. Sulfuric acid ( $H_2SO_4$ ), ammonium hydroxide ( $NH_4OH$ , 28-30%), nitric acid ( $HNO_3$ ) were attained from Daejung Chemicals. The as received analytical reagents (AR) were applied further without distillation.

#### **Synthesis of hexaaminobenzene (HAB)**

Hexaaminobenzene was prepared by a one-step amination reaction according to our previously reported procedure with slight modifications. First, chloroanilic acid (0.5 g) was taken in a high-pressure vessel placed in an ice bath, followed by adding of ethylenediamine (5 g) and sulfuric acid (few drops) under continuous stirring for 10 min. The obtained reaction mixture was stabilized to warm up to room temperature and then autoclaved for 80 °C for 12 h for completion of the amination reactions in Teflon container. Following with natural cooling, the brownish-black hexaaminobenzene complex was collected by vacuum filtering and rinsed with diethyl ether and degassed ethanol three times. The obtained product was freeze-dried for 24 h for further design of experiments. The all reactions were conceded in a Teflon container (50 mL) with autoclaving process.

#### **Synthesis Iron (II) nitrate precursor**

Iron (II) oxide (2.5 g) was dissolved in 7 g of nitric acid under vigorous stirring and allowed for complete dissolution of iron oxide. After that, the obtained product was collected, filtered, and washed with deionized water more than three times. Finally, the achieved solids were dried overnight and used for further experiments.

#### **Synthesis of Mn/Fe-Hexaiminobenzene Metal–Organic Frameworks (Mn/Fe-HIB-MOFs)**

M-HIB-MOFs were fabricated using sequential amination, protonation, and oxidation reactions. In typical experiments, manganese (II) nitrate and iron (II) nitrate were liquefied in 5 mL of N,N-dimethylformamide and deionized water (1:1 v/v) solution containing TX-100 with continuous mixing in the ice bath for 0.25 h to attain homogeneous solution, followed

by injection of appropriate amount of concentrated ammonium acetate/hydroxide and deoxygenated ethylenediamine. After that, a solution of hexaaminobenzene in 1-methyl-2-pyrrolidinone was poured into the above reaction mixture and was maintained for 70 °C for 2 h without stirring. Then, reacted at 100 °C for 7 h in Teflon autoclaving. After that, the Teflon-lined autoclave reactor was cooled to room temperature. The resulting precipitate was collected by filtering, centrifuging, and then rinsed with deionized water and ammonia solution three times. The obtained solid powders were dried overnight on a Schlenk line under vacuum. Finally, the as-prepared solids were annealed sequentially for 100 and 300 °C for 1 h with a nitrogen environment. Calculated elemental analyses of Mn/Fe-HIB-MOF: C: 28.20%, N: 33.59%, H: 2.38%, Mn: 17.88% and Fe: 17.95%. Found: C: 27.92%, N: 32.43%, Mn: 17.59% and Fe: 17.35%.

### **Synthesis of Mn-HIB-MOF and Fe-HIB-MOF**

Mn-HIB-MOF and Fe-HIB-MOF were prepared using a similar process to that of Mn/Fe-HIB-MOF, except for the use of iron (II) nitrate and manganese (II) nitrate reagents, respectively. The concentration of the metallic precursor was fixed constant (0.2 mmol).

Calculated elemental percentages for Mn-HIB-MOF: C: 27.90%, N: 33.19%, H: 2.35%, and Mn: 36.53%. Found: C: 27.76%, N: 32.21%, and Mn: 35.47%.

Calculated elemental percentages for Fe-HIB-MOF: C: 28.80%, N: 32.89%, H: 2.42%, and Fe: 35.89%. Found: C: 27.92%, N: 32.10%, and Fe: 35.19%.

### **Synthesis of Pt/C catalysts**

Poly(N-vinyl-2-pyrrolidone) ( $M_w = 40,000$ ) was added in the appropriate quantity of chloroplatinic acid ( $H_2PtCl_6 \cdot 6H_2O$ ) solution with vigorous stirring for 10 min, followed by the addition of activated carbon with continuous stirring. Then, a solution of sodium borohydride ( $NaBH_4$ ) appended to the reaction mixture and kept under stirring for another 30 min. Finally, the obtained mixture underwent multiple washings by deionized water with centrifugation and dried overnight under vacuum for 60 °C. The Pt mass loadings of  $\sim 0.15 \text{ mg cm}^{-2}$  was obtained by controlling the concentration of chloroplatinic acid, equivalent to those of M-HIB-MOFs catalysts.

### **Synthesis of the RuO<sub>2</sub> catalysts**

First, ruthenium (III) chloride (50 mM) was mixed with solutions of methyl alcohol and water (1:1 v/v) under vigorous stirring. Next, a solution of sodium hydroxide (NaOH, 2 M) appended dropwise in the obtained reaction mixture until the pH of solution became 7. The obtained product was centrifuged, rinsed with deionized water, and dehydrated for 60 °C, followed by annealing for 500 °C for 5 h in air.

### **Fabrication of functionalized bio-cellulose membrane electrolytes:**

The bagasse of sugarcane was cleansed by dispersion in deionized water, NaOH, and nitric acid in ethanol (20% v/v, refluxing, three times), followed by filtering and multiple washings with deionized water until neutral pH of the drained water. The obtained bagasse was dried for 3 h at 100 °C and grinded in 16-mesh IKA MF-10 mill with SS sieves. The fiber pulp was bleached with hydrogen peroxide at 55 °C for 1 h, and the reaction was replicated three times for 3 h. After filtration, the residue was treated with NaOH solution for 3 h for ambient temperature. The resultant solution was collected by filtering and multiple washing by deionized water until a neutral pH was obtained. Furthermore, these fibers were rinsed with ethanol and acetone and dried for 6 h at 50 °C with air circulation. The whitened fibers were treated with enzymatic hydrolysis with a combination of hemicell/pectinase (Viscozyme® L) and endoglucanase enzymes (FiberCare® R). These enzymes showed the collective influence of endocellulase and beta-glucanase [endo-1,3(4)] cleavages. The practical dosages of enzymes with biomass were 0.1 and 0.33 mg/g for Viscozyme® L and FiberCare® R, respectively. The hydrolysis reactions were conducted with sodium citrate buffer solutions for 72 h at 50 °C with an orbital shaker. After that, the hydrolysis reactions were stopped by boiling the reaction mixture for 10 min, followed by sonication and freeze drying. These enzyme-derived fibers were redispersed in the distilled water with a sonifier (S-450) for 20 min with a pulse rate of 10 s, and placed in an ice bath to obtain cellulose nanofibers.

The methyl and carboxymethyl groups were functionalized to the obtained cellulose. Cellulose nanofibers (3 g) were dissolved in 100 mL solution consisting of deionized water (81% w/v), urea (12% w/v), and sodium hydroxide (7% w/v) with continuous stirring for 1.5 h for 100 °C, to obtain alkali-cellulose slurry. The slurry was frozen for 0 °C, and thawed at room temperature to gain a cellulose solution. Next, a solution of monochloroacetic acid in ethanol and dimethyl sulfate in acetone appended sequentially at ambient environment. The

reactant mixture was further transferred to a water bath for 5 min for 50 °C, followed by neutralization by acetic acid (10%), ensuring the removal of excess NaOH. The cellulose was recovered by filtration and washing with methanol/acetone for 6 times and exposed for drying for 6 h at 50 °C. The obtained cellulose was cross-linked with chitosan. Typically, chitosan and glutaraldehyde were dissolved in water, and the resultant celluloses was then poured in the solution under continuous stirring for 3 h at 50 °C. Next, the unreacted chemicals were removed by multiple washing with deionized water and stowed for 4 °C.

The functionalization of cross-linked cellulose nanofibers was conducted with choline chloride. The nanofibers were homogeneously dispersed in deionized water. First, 10% choline chloride was added in the fiber suspension with continuous rousing for 12 h at ambient environment. The resulting suspension was collected by filtering and multiple rinsing by ethanol and deionized water, ensuring the removal of traces of choline chloride. Next, the functionalized bio-cellulose membrane was prepared by a phase inversion method. Typically, cellulose (3 g) was mixed in dichloromethane under stirring for 1 h, followed by sonication for 10 min to ensure the removal of air bubbles. The solution was casted on glass board, and then immersed in deionized water for 2 h at 4 °C, to release the membrane. The membrane was placed for cross-linking under vacuum for 24 h at 60 °C. The obtained bio-cellulose membranes (50–1000  $\mu\text{m}$ ) were exchanged with hydroxide groups in the KOH aqueous solution (1 M) for 24 h. Lastly, the resulting membranes were collected by washing and soaking in deionized water.

### **Characterization of the prepared catalysts**

Nitrogen atmosphere was utilized for all air- and water-sensitive experiments. Powder X-ray diffraction (PXRD) patterns were measured by using Advanced Photon Source (APS), 11-BM beamline with a wavelength of 0.517045 Å. The obtained PXRD patterns were background-corrected by Bruker Diffractometer software. The diffraction intensities and unit cell parameters were extracted by Pawley fitting. *In situ* PXRD patterns were analyzed on Rigaku Smartlab with a wavelength of 1.5406 Å. Field-emission scanning electron microscopy (FESEM) was conducted on a JEOL-6700F to obtain the surface morphology and structures. Transmission electron microscopy (TEM) images were acquired on a Cs-corrected Titan<sup>TM</sup> 80-300 with an accelerating voltage of 300 kV. Powder dispersed ethanol solutions were drop-casted on the Cu TEM grids. Elemental distribution maps were recorded by an EDS attached to the TEM. Atomic modulations were determined on the scanning tunneling

microscopy (SPECS JT-STM) system in UHV mode. The nitrogen sorption measurements were conducted on an AUTOSORB-1-MP surface area and pore size analyzer using a liquid nitrogen bath (77 K). The surface volume, area, and pore profiles were analyzed from the adsorption and desorption branches by the Brunauer–Emmett–Teller (BET) and Barrett–Joyner–Halenda (BJH) methods. FTIR measurements were performed on a Perkin Elmer GX spectrometer. Thermogravimetric analysis (TGA) was measured on TA Instruments Q500 TG analyzer with a heating rate of 1 °C/min. X-ray photoelectron spectroscopy (XPS) was performed on a VG SCIENTA (R 3000) spectrometer equipped with a monochromatic Al K $\alpha$  source. Mn and Fe K-edge XAFS spectra were performed under the transmission mode of synchrotron radiation source at room temperature. The obtained energy was calibrated using metal foils of Mn and Fe. The Fourier transform was analyzed by using Bessel functions. The electrical conductivity was measured by performing the van der Pauw technique. The prepared MOFs powder was pressed in the pellets by using a pressing die with hydraulic pump for 30 min. The thickness of the pellets was analyzed by using a micrometer screw gauge. The obtained pellets were placed onto dry aluminum oxide. Further, four gold wires at four corners using carbon paste connected the pellets and the other end of the gold wires pasted onto dry aluminum oxide. The obtained device was placed on to the respective probes.

### **Electrochemical measurements**

The electrochemical performances were performed on an electrochemical workstation (CHI 760 D, CH Instruments) at room temperature with a typical three-electrode electrochemical cell. It includes, a Ag/AgCl (with saturated KCl) reference electrode, a platinum wire as the counter electrode, a glassy carbon (GC) rotating disk electrode (RDE, 0.196 cm<sup>2</sup>) coated with the catalysts as the working electrode, and 0.1 M aqueous KOH (oxygen rich) as the electrolyte. The observed potentials and current densities were standardized to the reversible hydrogen electrode (RHE) according to the Nernst equation ( $E_{\text{RHE}} = E_{\text{Ag/AgCl}} + 0.059 \times \text{pH} + 0.205$ ) and the geometric surface area, respectively. The catalysts inks were prepared by dispersing 10 mg of the catalysts and 50  $\mu\text{L}$  Nafion (5 wt%) into isopropyl alcohol (1.95 mL). Then, 6  $\mu\text{L}$  of the prepared inks were evenly loaded on a glassy carbon electrode and dried overnight for room temperature to obtain 0.15 mg cm<sup>-2</sup> mass loadings. Pt/C and RuO<sub>2</sub> were considered as references catalysts with equivalent mass loadings. Note that the mass loadings were similar for both oxygen reactions unless otherwise mentioned. Prior to the

ORR/OER measurements, the electrolyte (0.1 M KOH) was saturated by oxygen, nitrogen flow for 30 min. CVs were performed in O<sub>2</sub> and N<sub>2</sub>-saturated electrolyte with a scan rate of 50 mV s<sup>-1</sup>. LSV profiles for ORR/OER were obtained for 1600 rpm with a scan rate of 5 mV s<sup>-1</sup> in the potential range of 0.2–2 V vs. RHE. The half-cell reaction stability was determined by measuring the chronoamperometric measurements at constant overpotential. Electrochemical impedance spectra were obtained for the frequency range of 100 Hz to 1 MHz with a constant bias of 0.2 V. The long-life durability of the catalysts was measured by continuous potentiodynamic sweeps for a scan rate of 100 mV s<sup>-1</sup>.

### Oxygen reduction reaction kinetics

The ORR kinetics were evaluated by using different rotational speed LSV profiles. The measured total current density is the sum of inverse of kinetic current ( $J_K$ ) and diffusion current ( $J_d$ ). Every atom or ion on the electrode reacts immediately as the applied overpotential is sufficiently high. The number of oxygen molecules at the electrode surface is almost zero, facilitating diffusion-limiting plateau. Therefore, the diffusion current is related only to the RDE rotational speeds.

The transferred electron number ( $n$ ) in oxygen reduction was determined according to the Koutecky–Levich (K–L) equation<sup>S1-S3</sup>:

$$\frac{1}{J} = \frac{1}{J_K} + \frac{1}{B\omega^{1/2}} \quad (\text{S1})$$

$$B = 0.2nF(D_{O_2})^{2/3}\nu^{-1/6}C_{O_2} \quad (\text{S2})$$

where  $B$  represents the Levich slope,  $J_K$  represents the kinetic current,  $J$  represents the measured total current,  $\omega$  represents the electrode rotation rate,  $n$  represents the number of electrons transferred for each oxygen molecule,  $F$  represents the Faraday constant ( $F = 96485$  C mol<sup>-1</sup>),  $D_{O_2}$  represents the O<sub>2</sub> diffusion coefficient in 0.1 M KOH ( $D_{O_2} = 1.9 \times 10^{-5}$  cm<sup>2</sup> s<sup>-1</sup>),  $\nu$  represents the kinetic viscosity (0.01 cm<sup>2</sup> s<sup>-1</sup>) and  $C_{O_2}$  represents the concentration of O<sub>2</sub> ( $C_{O_2} = 1.2 \times 10^{-6}$  mol cm<sup>-3</sup>). The considered rotation speeds are in rpm, and therefore, the constant factor 0.2 is multiplied. The peroxide species during ORR reactions were determined by measuring the RRDE polarization profiles for the ring potential of 1.3 V vs. RHE. Based on the following expressions, the transferred electron number ( $n$ ) and peroxide (H<sub>2</sub>O<sub>2</sub>) yield were evaluated as<sup>S4</sup>:

$$n = 4 \frac{I_d}{I_d + I_r/N} \quad (\text{S3})$$

and

$$H_2O^- (\%) = 100 \frac{2I_r/N}{I_d + I_r/N} \quad (\text{S4})$$

where  $I_r$  represents the ring current,  $I_d$  represents the disk current, and  $N$  represents the current collection efficiency of the Pt ring.  $N$  was determined to be 0.42.

## **Metal–Air Battery Performance**

### **Rechargeable liquid Zn–Air battery assembly**

The rechargeable Zn–air battery performance was analyzed on home-built electrochemical cells. Air cathodes were constructed by uniformly drop-casting M-HIB-MOFs slurry over carbon paper followed drying for room temperature for 12 h. The catalysts slurry was prepared by mixing carbon black, polytetrafluoroethylene, and the catalysts (1:1:8 w/w) in ethanol/Nafion solution. The mass loadings of the catalysts for rechargeable ZABs was 0.5 mg cm<sup>-2</sup>. The reference catalyst mixture was of Pt/C and RuO<sub>2</sub> with the mass ratio of 1:1. Here, 6 M KOH with 0.2 M zinc acetate was used as an electrolyte for the reversible electrochemical reactions. Catalyst-loaded carbon paper was used as an air cathode and polished Zn plate (0.5 mm thickness) as anode.

### **Bio-cellulose membrane electrolyte**

#### **Water content**

The water content of the fabricated membranes was determined according to the method of Jayme and Rothamel. The membranes were soaked in deionized water for 24 h for room temperature, centrifuged for 5 min ( $m_{\text{wet}}$ ), and dried for 100 °C until they reached a constant weight ( $m_{\text{dry}}$ ). The water content and swelling ratio were determined according to the expression:

$$\text{Water content} = (m_{\text{wet}} - m_{\text{dry}})/m_{\text{dry}} \times 100 \text{ and Swelling ratio} = (t_{\text{wet}} - t_{\text{dry}})/t_{\text{dry}} \times 100. \quad (\text{S5})$$

where  $t$  is the thickness of the membrane before and after drying.

### **Ion transport kinetics**

Electrochemical reactions in alkaline Zn–air batteries involved the transport of OH<sup>-</sup> and Zn<sup>2+</sup>, facilitating the key role in the ion conduction mechanism. The transfer numbers of OH<sup>-</sup>, K<sup>+</sup>, Zn<sup>2+</sup>, and CH<sub>3</sub>COO<sup>-</sup> were calculated according to the expression below:

$$t_i = z_i \mu_i C_i / \sum_i z_i \mu_i C_i \quad (\text{S6})$$

where  $z_i$  represents the valence charge,  $\mu_i$  the ion mobility, and  $C_i$  the ion concentration of  $i$ .

### **Ion conductivity and activation energy**

The ionic conductivity of the fabricated functionalized bio-cellulose membrane was determined by the following expression, using an AC impedance technique (electrochemical workstation CHI 760 D, CH Instruments, frequency range 1 MHz to 1 Hz):

$$\sigma = L/RA \quad (\text{S7})$$

where  $\sigma$  is the ionic conductivity,  $A$  is the cross-section area,  $R$  the measured resistance, and  $L$  is the distance between reference and working electrodes.

The activation energy was calculated by the Arrhenius equation as follows:

$$\sigma = A \times \exp(-E_a/RT), \text{ where } E_a \text{ is the activation energy.} \quad (\text{S8})$$

### **Rechargeable solid-state Zn–Air battery assembly**

The all-solid-state flexible Zn–air batteries were designed by including Mn/Fe-HIB-MOF comprised catalysts on stainless steel (SS) mesh as the air cathode, the functionalized bio-cellulose nanofibers membrane (fabricated as per procedure shown above) as the solid electrolyte, and Zn-foil (patterned) as the anode. Then, the SS mesh with catalysts and zinc foil were positioned on opposite sides of the bio-cellulose membrane electrolyte, without any external current collector. Finally, the assembled devices were pressed cautiously and encapsulated with sustainable latex.

### **Battery testing**

All the designed batteries were evaluated under atmospheric conditions. The galvanostatic discharging and charging voltage profiles were conducted on a LAND CT2001A multichannel battery testing system. The cycling for aqueous batteries was performed for 10 min per cycle (discharge: 5 min; charge: 5 min) with 10 mA cm<sup>-2</sup> current density. The all-solid-state batteries were cycled for 10 min per cycle at the current density of 25 mA cm<sup>-2</sup>. The specific capacities were determined using the galvanostatic discharge profiles

standardized to the consumed mass of Zn. The energy efficiency was calculated from the ratio of discharge to charge voltages. The power densities of both ZABs were calculated by expression as  $P = V \times I$ .

### Supplementary Figures

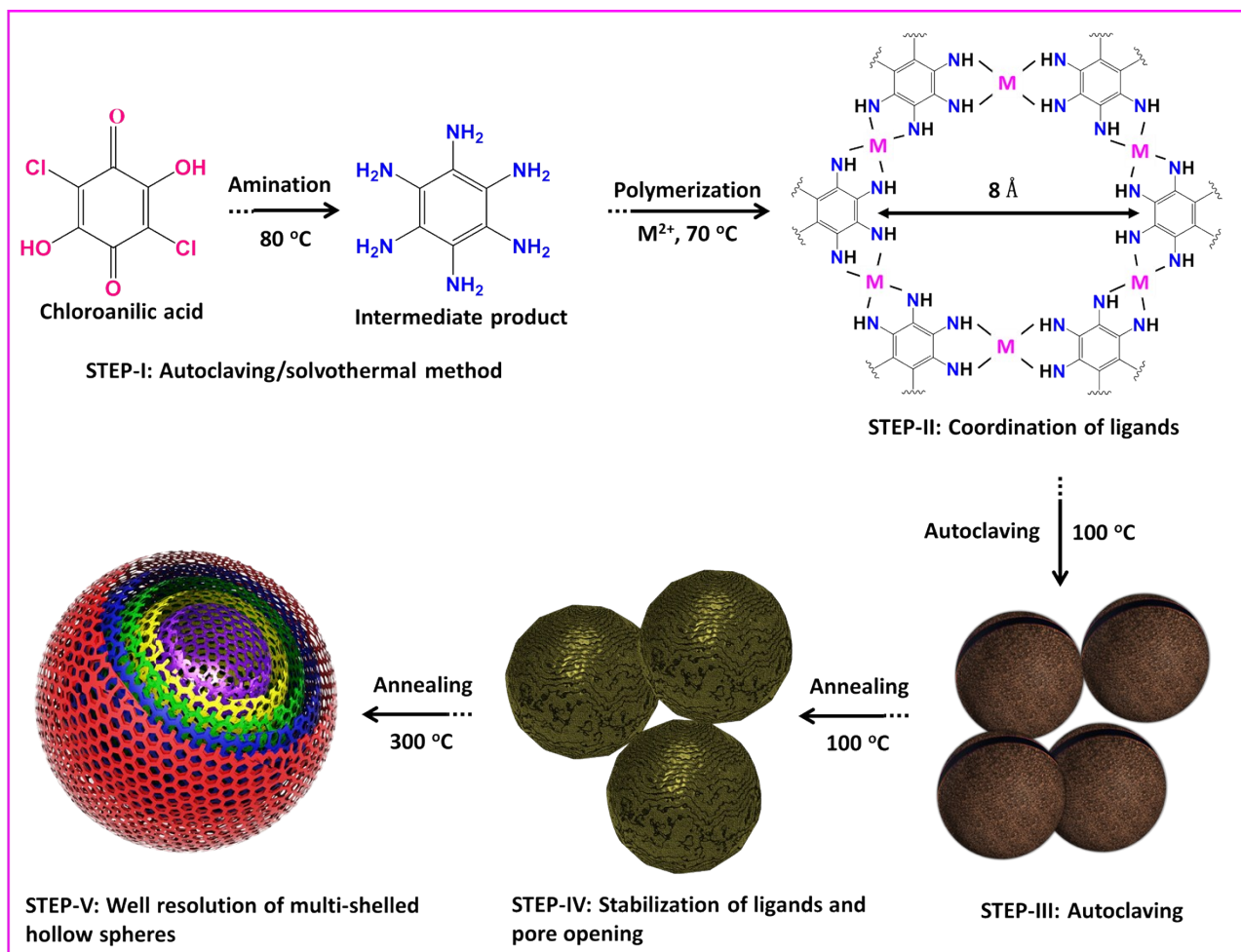


**Figure S1.** Growth mechanism of multishelled hollow spheres of Mn/Fe-HIB-MOF with pore size of  $\sim 8 \text{ \AA}$ .

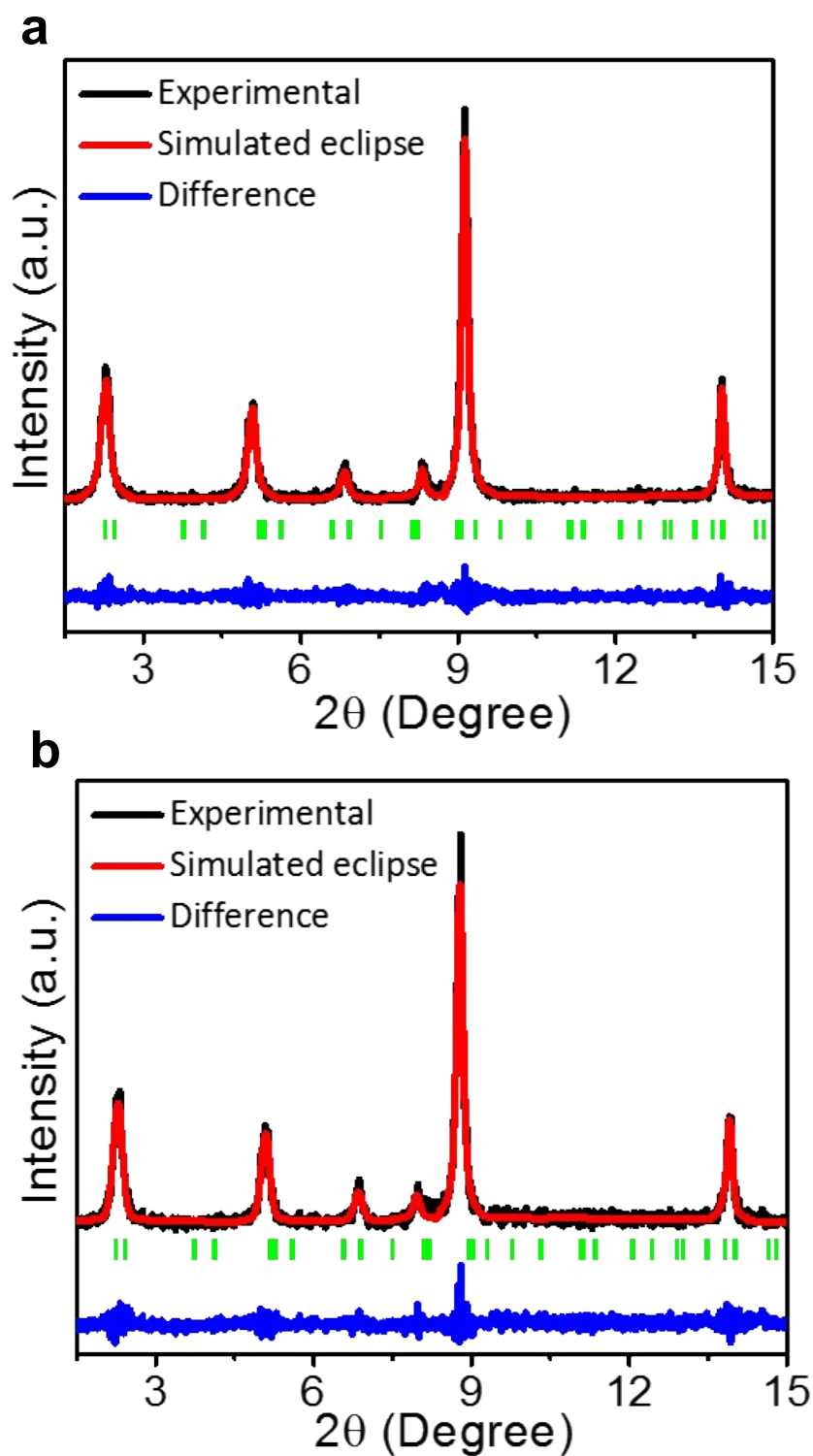


**Figure S2.** Pawley fitting of the powder XRD patterns of (a) Mn-HIB-MOF and (b) Fe-HIB-MOF catalysts. Pawley refinements yield unit cell parameters for Mn-HIB-MOFs ( $a = b = 13.28 \text{ \AA}$  and  $c = 3.14 \text{ \AA}$ ,  $\alpha = 90.0^\circ$ ,  $\beta = 90.0^\circ$ , and  $\gamma = 120.0^\circ$ ,  $R_p = 0.325$ ,  $R_{wp} = 0.0402$ ,  $R_{exp} = 0.0133$ ,  $GOF = 3.022$ ) and Fe-HIB-MOF ( $a = b = 13.30 \text{ \AA}$  and  $c = 3.18 \text{ \AA}$ ,  $\alpha = 90.0^\circ$ ,  $\beta = 90.0^\circ$ , and  $\gamma = 120.0^\circ$ ,  $R_p = 0.359$ ,  $R_{wp} = 0.0436$ ,  $R_{exp} = 0.0119$ ,  $GOF = 3.66$ ).

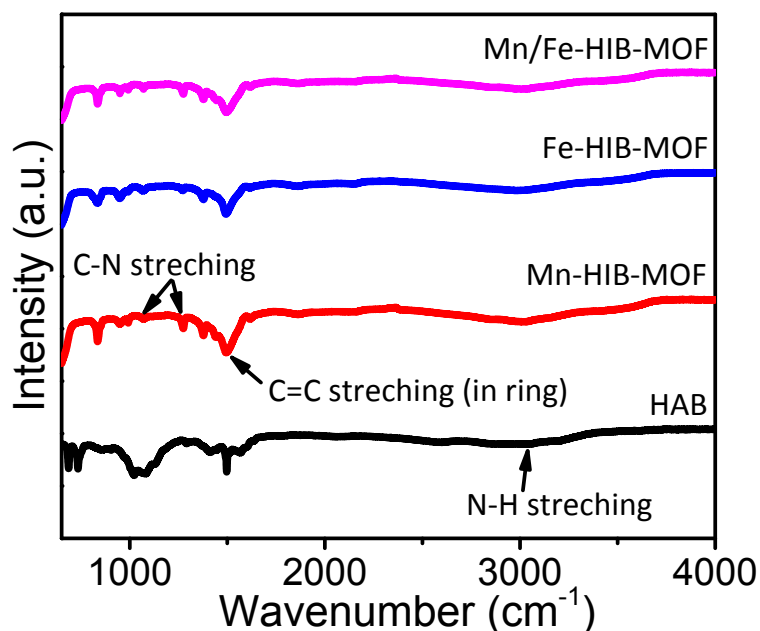


**Figure S3.** Fourier transform infrared (FTIR) spectra of the HAB, Mn-HIB-MOF, Fe-HIB-MOF, and Mn/Fe-HIB-MOF catalysts.

Molecular structures of M-HIB-MOFs were determined using FTIR spectra. HAB displays two peaks in the range of 2500–2800  $\text{cm}^{-1}$ , reflecting the presence of HCl (<https://webbook.nist.gov/cgi/cbook.cgi?ID=C7647010&Type=IR-SPEC&Index=1>), whereas the absence of HCl peak in the N-HIB-MOFs confirms the formation of stable MOFs.<sup>S5,S6</sup> The characteristic broad peak of N-H stretch vibrations is observed in the range of 3000–3500  $\text{cm}^{-1}$  for the M-HIB-MOFs and HAB precursor, showing presence of amine groups.<sup>S7</sup> Furthermore, the peaks observed in the range of 1000–1400  $\text{cm}^{-1}$  corresponded to the stretched vibrations of C-N bonds (pyridinic, pyrrolic, and graphitic nitrogen species). The strong peak of C=C stretching mode in the ring structure was observed at 1495  $\text{cm}^{-1}$ ,<sup>S8</sup> revealing the successful formation of metal-based hexaaminobenzene metal-organic frameworks (M-HIB-MOFs). The obtained C=C and C-N vibrations are well agreed with XPS measurements. The electron-donating groups of aromatic rings (e.g., ortho, para, and meta) show presence of vibrations at  $\sim 837 \text{ cm}^{-1}$  in the Mn-HIB-MOF, Fe-HIB-MOF, and Mn/Fe-HIB-MOFs catalysts, suggesting the probability for fast electron transfer. Mn-HIB-MOF, Fe-HIB-MOF, and Mn/Fe-HIB-MOF showed a weak signal at  $\sim 2146 \text{ cm}^{-1}$ , recognized to the N=C=N or N=C=O stretched vibrations because for pyridinic  $\text{N}^+\text{O}^-$  species, which is consistent with XPS analysis.<sup>S9</sup> FTIR analysis confirms the successful construction of such kind of metal-organic frameworks.

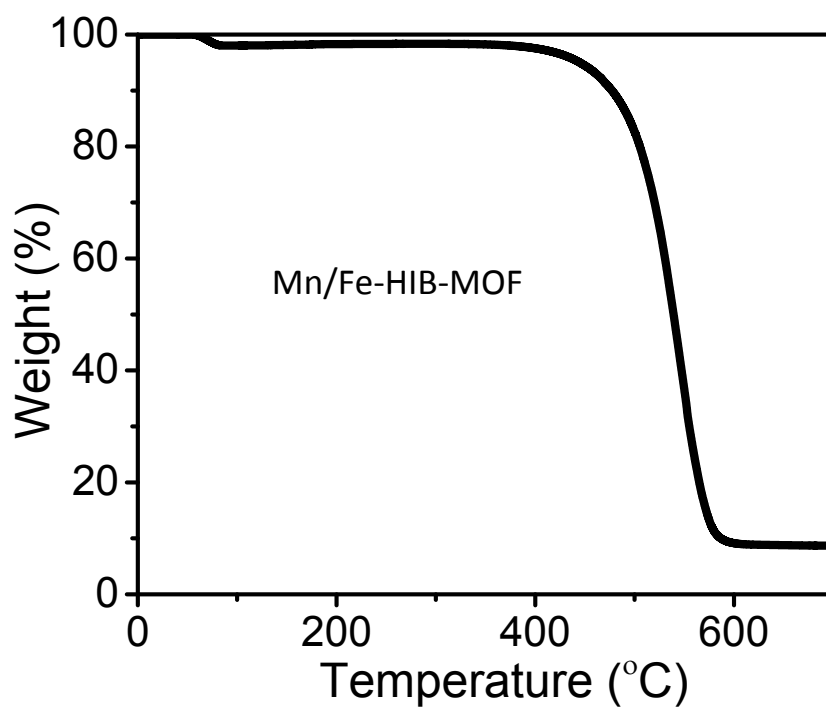


**Figure S4.** Thermogravimetric (TG) analysis for Mn/Fe-HIB-MOF catalyst.

The prepared Mn/Fe-HIB-MOFs catalysts examined the desolvation over  $\sim 400$  °C and likely to decompose above  $\sim 500$  °C with pronounced weight loss from up to  $\sim 600$  °C. This confirms the outstanding thermal stability of hexagonal unit cells of prepared metal–organic frameworks.

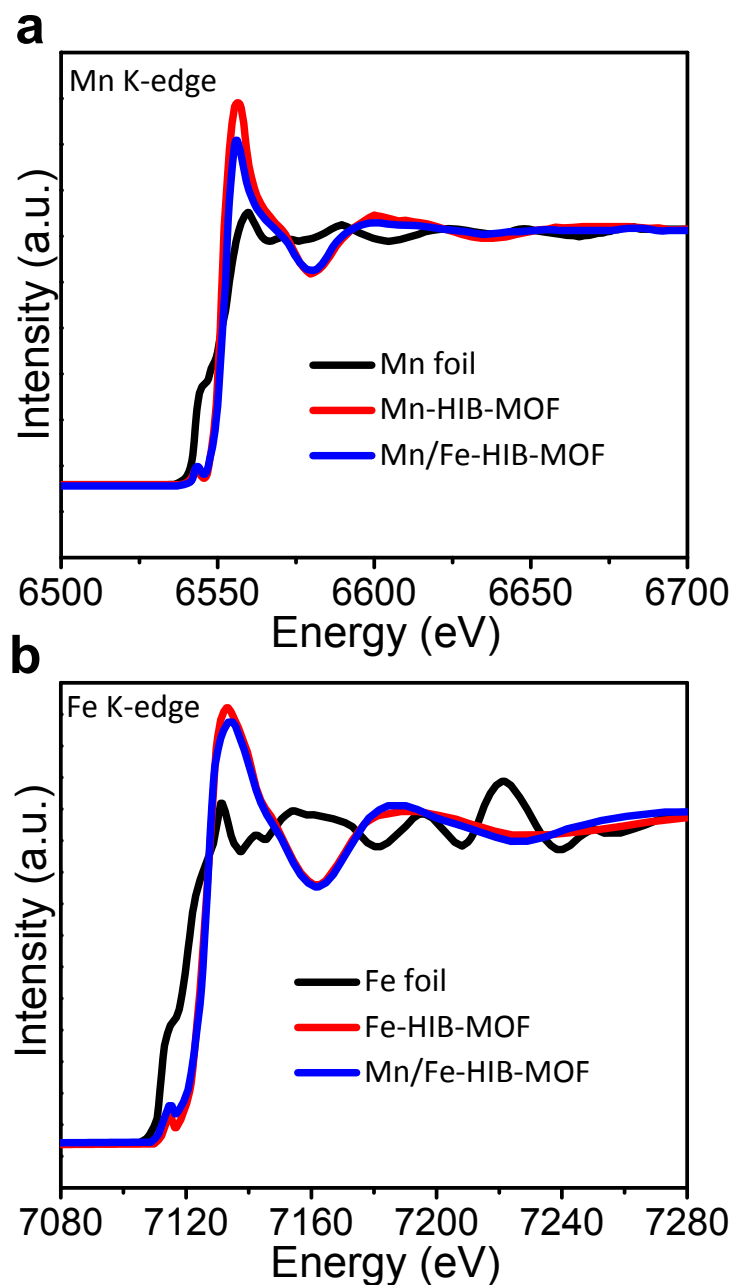


**Figure S5.** Chemical states and coordination structure analysis of the prepared metal–organic frameworks (M-HIB-MOFs). (a) Mn K-edge X-ray absorption near-edge structure (XANES) spectra of Mn foil, Mn-HIB-MOF, and Mn/Fe-HIB-MOF. (b) Fe K-edge XANES spectra of Fe-HIB-MOF and Mn/Fe-HIB-MOF catalysts compared with Fe foil.

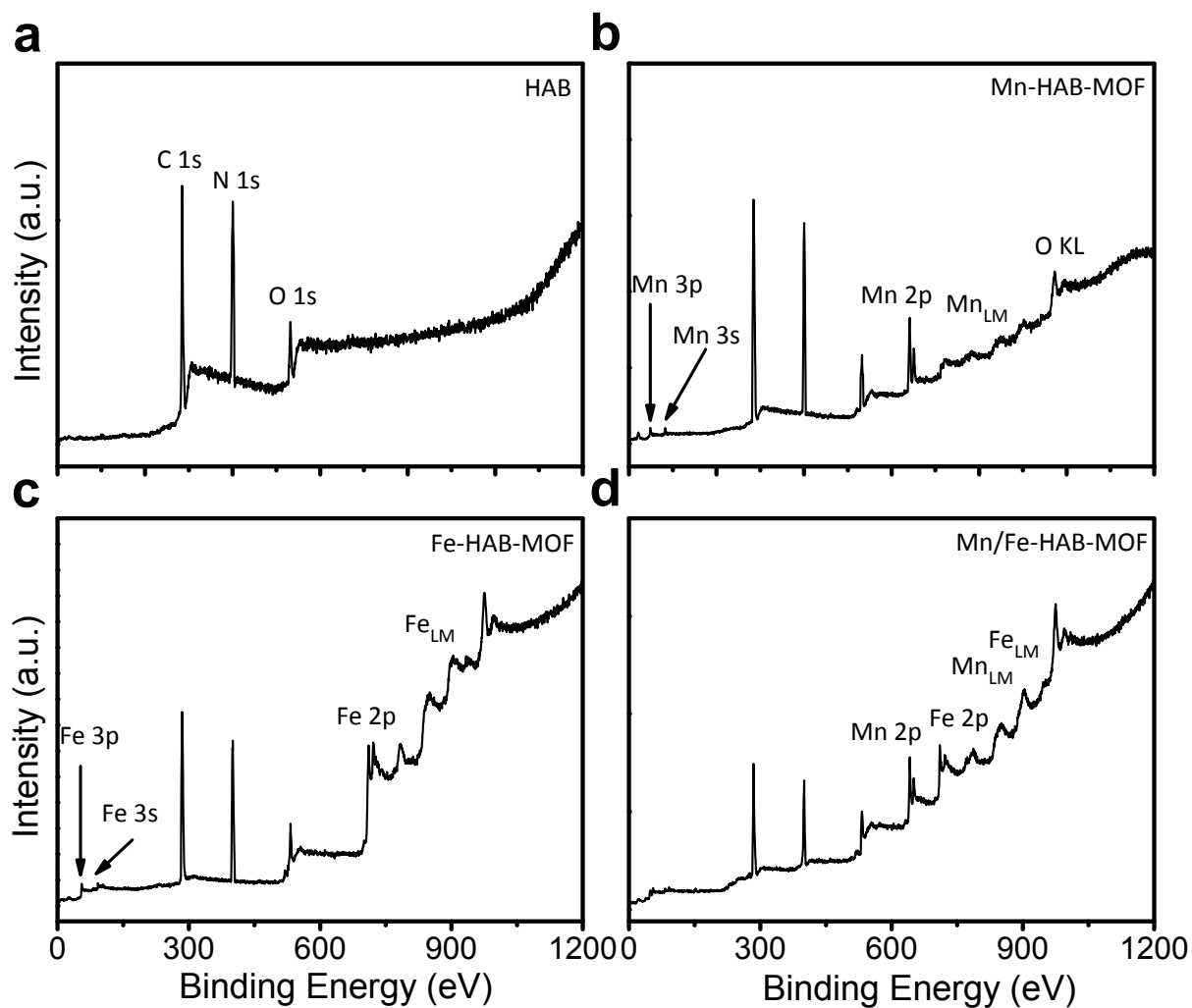


**Figure S6.** XPS survey spectra of metal–organic frameworks (a) HAB, (b) Mn-HIB-MOF, (c) Fe-HIB-MOF, and (d) Mn/Fe-HIB-MOF catalysts.

It shows the presence of C, N, O, Mn, and Fe and the absence of charge-balancing cations and anions such as  $\text{NH}_4^+$  and  $\text{Cl}^-$ , illustrating the neutral structure of MOFs.

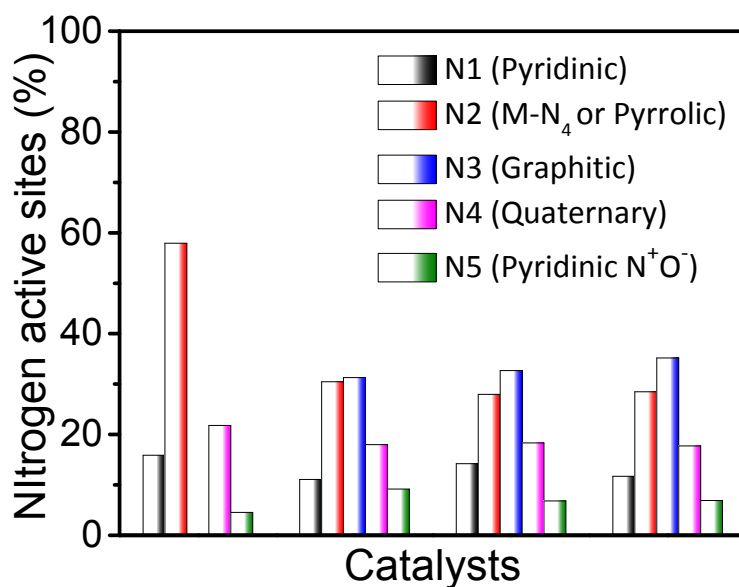


**Figure S7.** Quantitative distribution percentages of the nitrogen moieties with total nitrogen contents for the HAB, Mn-HIB-MOF, Fe-HIB-MOF, and Mn/Fe-HIB-MOF catalysts.

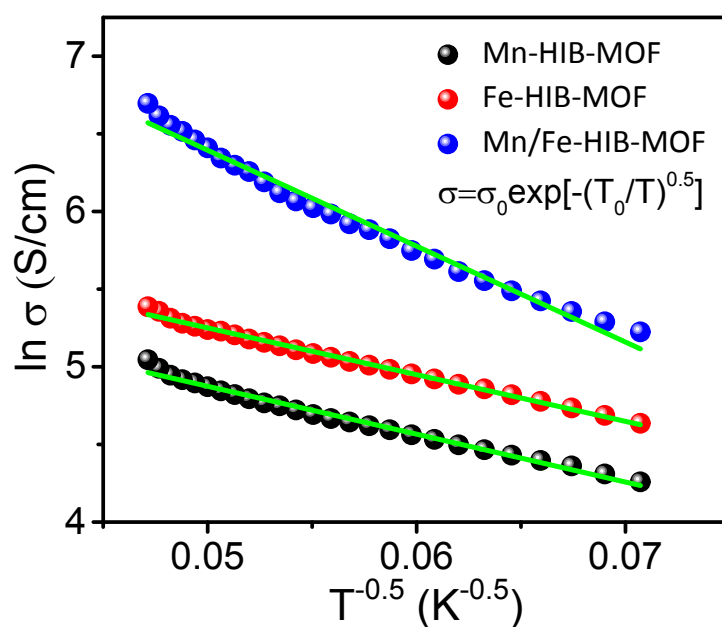


**Figure S8.** Conductivity of the prepared Mn-HIB-MOF, Fe-HIB-MOF, and Mn/Fe-HIB-MOF catalysts as a function of the inverse of the temperature based on granular metal model fitting. The equation used for fitting is  $\sigma = \sigma_0 \exp[-(T_0/T)^{0.5}]$ , where  $\sigma$  is the electrical conductivity,  $T$  is the absolute temperature, and  $\sigma_0$ ,  $T_0$  are constants.

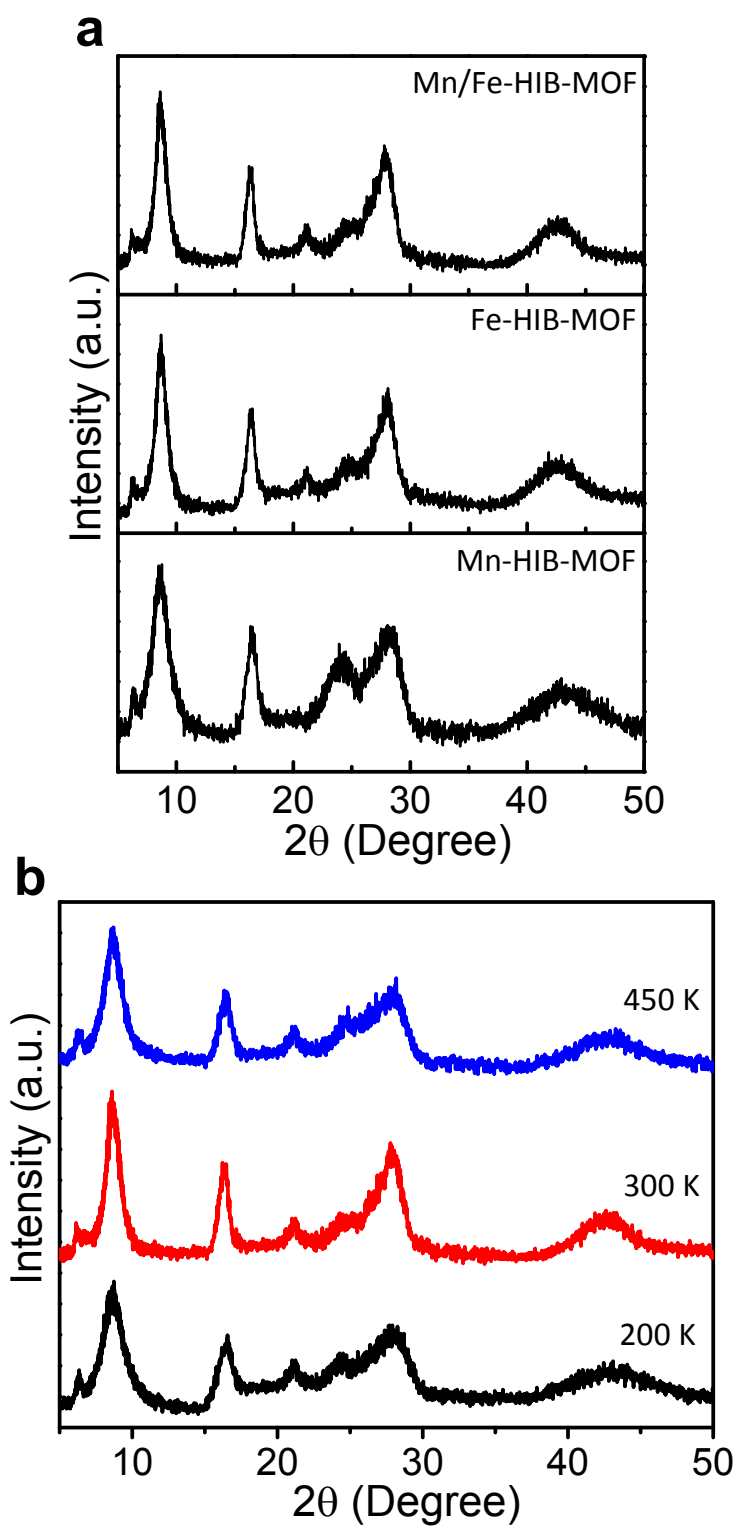


**Figure S9.** (a) *In situ* Powder XRD patterns of Mn-HIB-MOF, Fe-HIB-MOF, and Mn/Fe-HIB-MOF catalysts at room temperature (300 K). (b) *In situ* PXRD patterns of Mn/Fe-HIB-MOF for different temperatures of 200, 300, and 450 K. (Wavelength: 1.5405 Å)

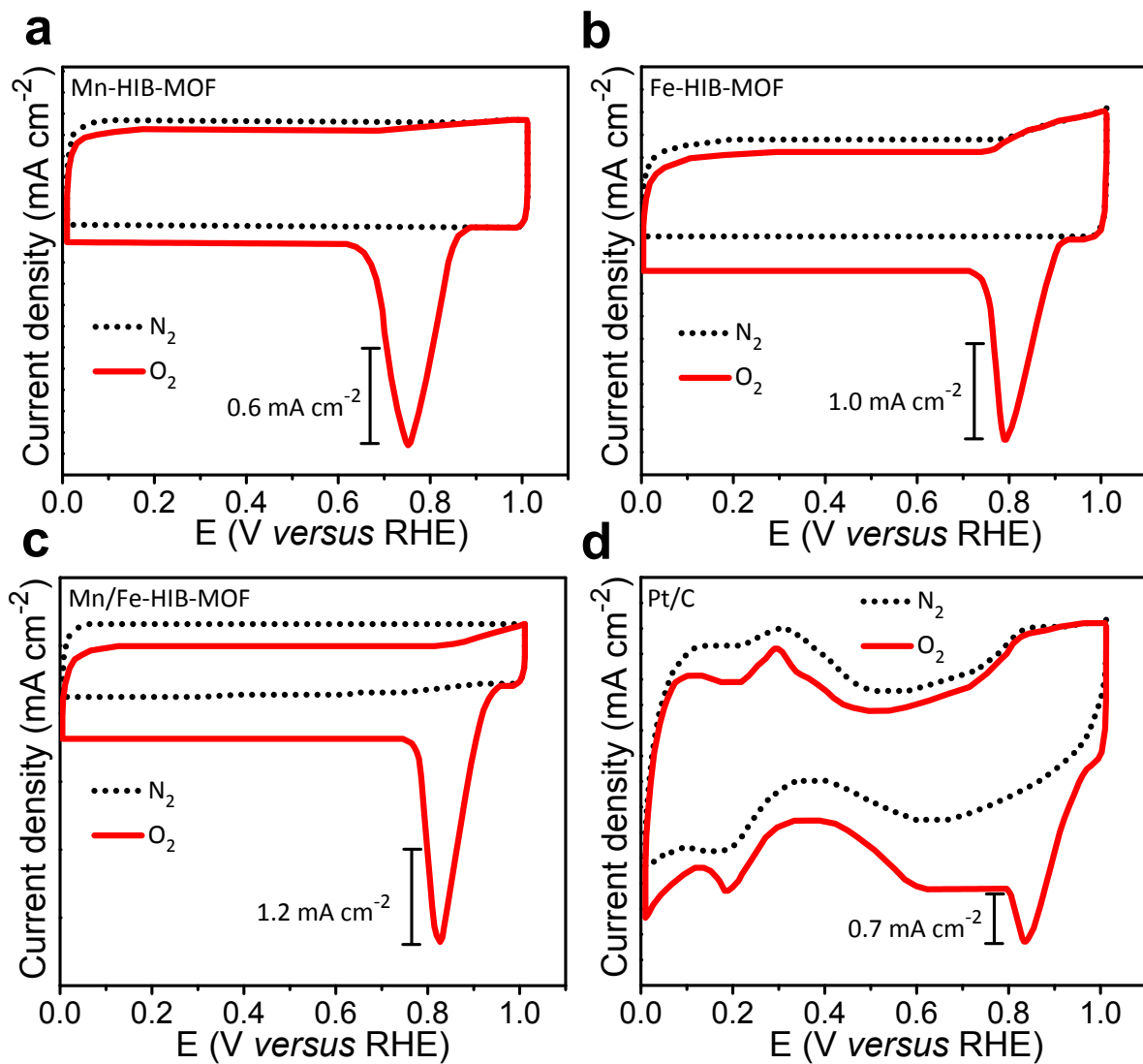


**Figure S10.** Cyclic voltammograms for (a) Mn-HIB-MOF, (b) Fe-HIB-MOF, (c) Mn/Fe-HIB-MOF, and (d) Pt/C catalysts in N<sub>2</sub>-saturated (black dotted lines) and O<sub>2</sub>-saturated (red solid lines) aqueous 0.1 M KOH solution.

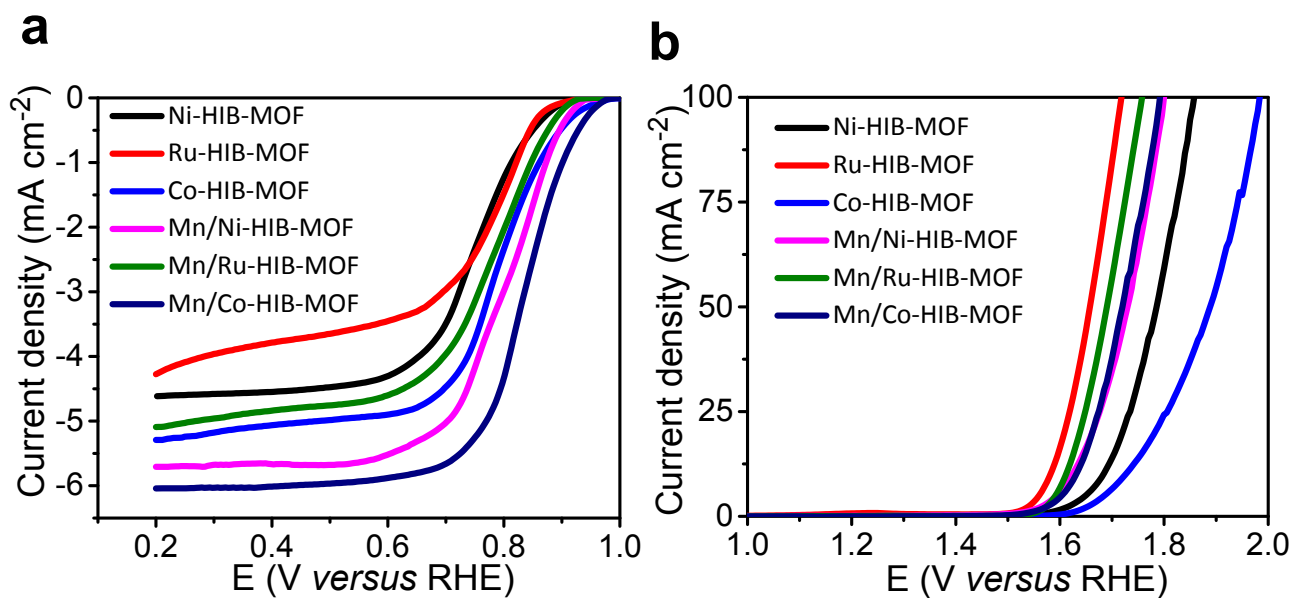


**Figure S11.** RDE polarization profiles of various transition metal-based MOF (Co, Ni, Ru, and their combinations) for the (a) ORR and (b) OER.

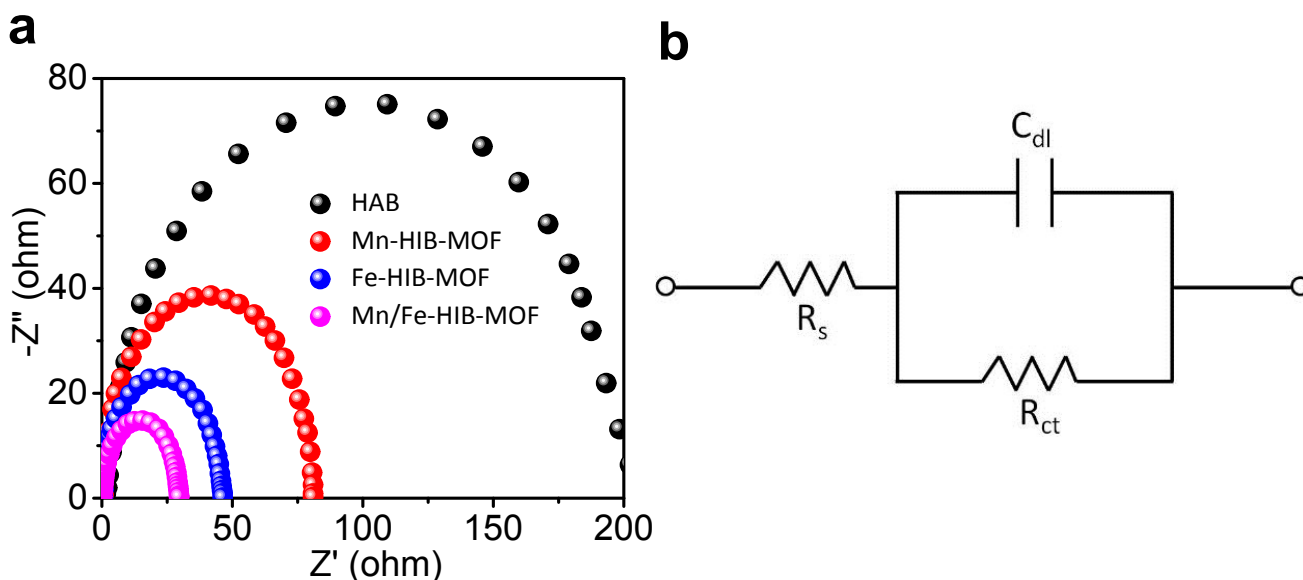


**Figure S12.** (a) Electrochemical impedance spectra (EIS) of the HAB, Mn-HIB-MOF, Fe-HIB-MOF, and Mn/Fe-HIB-MOF catalysts for ORR obtained in 0.1 M KOH, and (b) their analogous equivalent circuit. The lower charge transfer resistance is confirmed by the presence of smaller diameter of semicircle of Mn/Fe-HIB-MOF than those of HAB, Mn-HIB-MOF, and Fe-HIB-MOF, illustrating superior electrocatalytic performance.

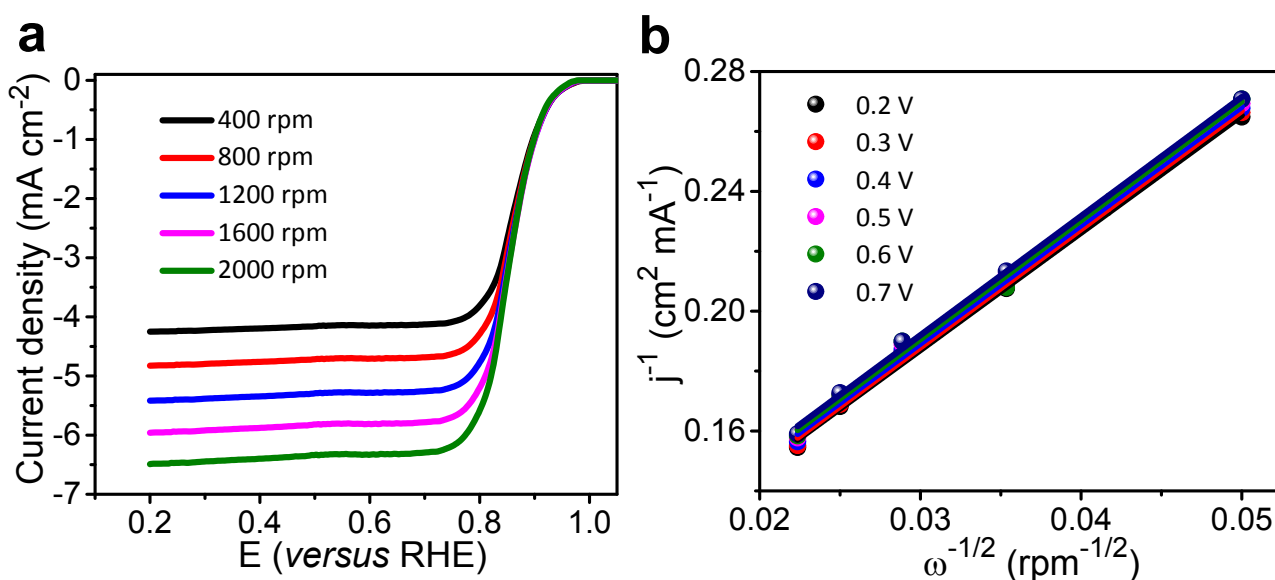


**Figure S13.** (a) RDE polarization profiles of Pt/C for the ORR. (b) Representative K–L plots for different potentials including transferred electron number. ( $n = 3.76$ )

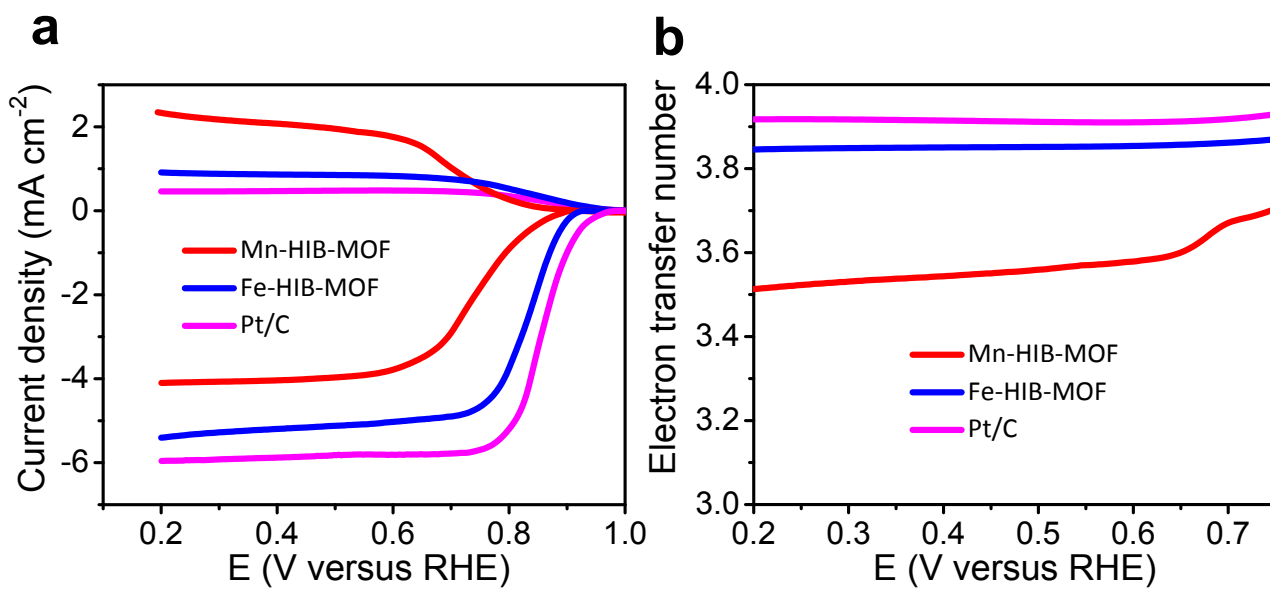


**Figure S14.** (a) Ring and disk polarization profiles of Mn-HIB-MOF, Fe-HIB-MOF, and Pt/C for the ORR and (b) their mean transfer numbers. (Conditions: 0.1 M KOH)

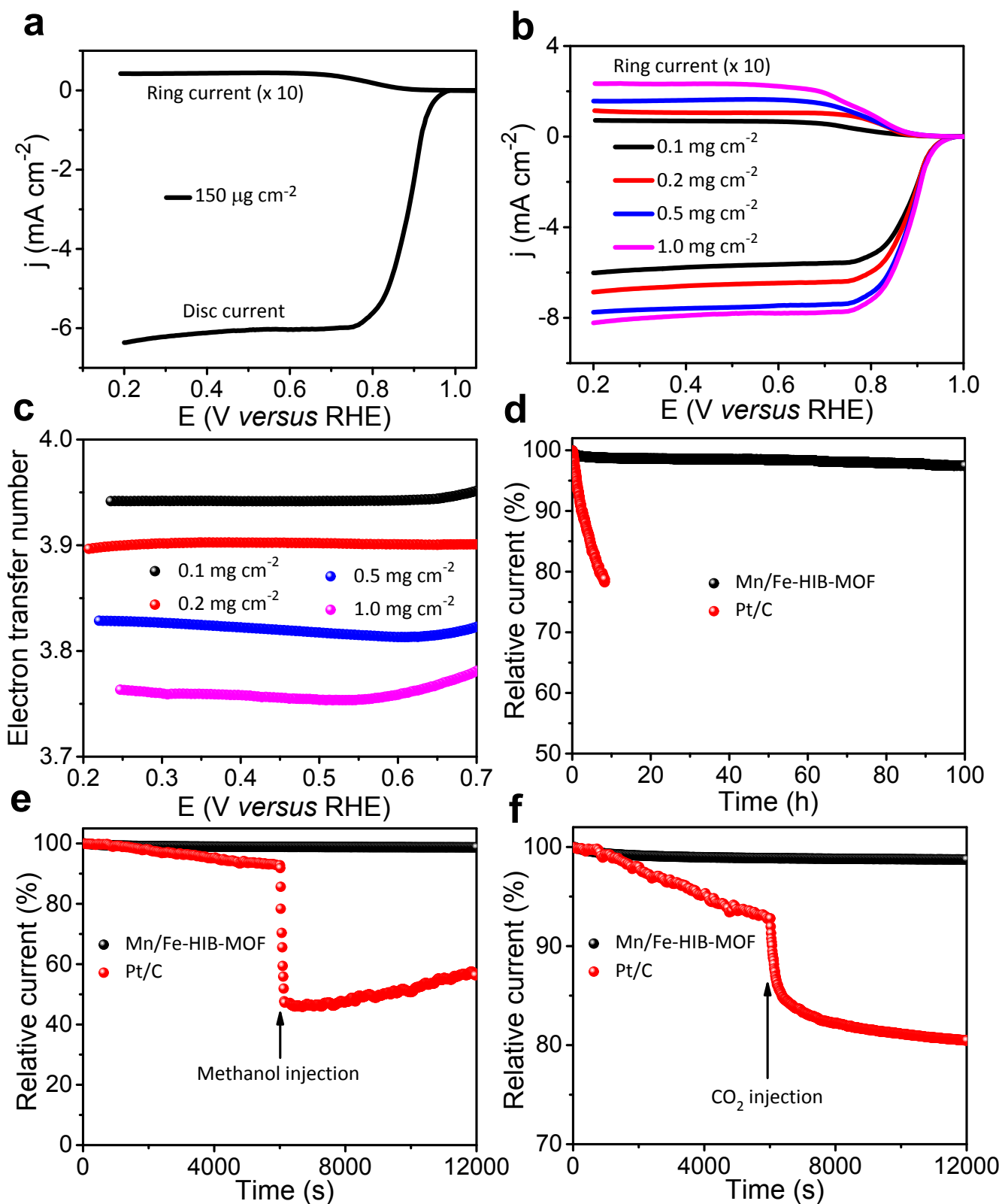


**Figure S15.** (a) RRDE polarization profiles for Mn/Fe-HIB-MOF at 1600 rpm with  $150 \mu\text{g cm}^{-2}$  mass loading during ORR. (b) RDE polarization plots of Mn/Fe-HIB-MOF at different mass loadings ( $0.15$  to  $1 \text{ mg cm}^{-2}$ ) and (c) corresponding mean transfer numbers. The stability tests for ORR: (b) ORR examination by  $I-t$  chronoamperometric stability responses of

Mn/Fe-HIB-MOF and Pt/C catalysts. (c)  $I-t$  stability response before/after methanol injection (2 M) tests. (d)  $I-t$  stability tests before/after introduction of CO (10 volume %) into the electrolyte. (Conditions: 0.1 M KOH)

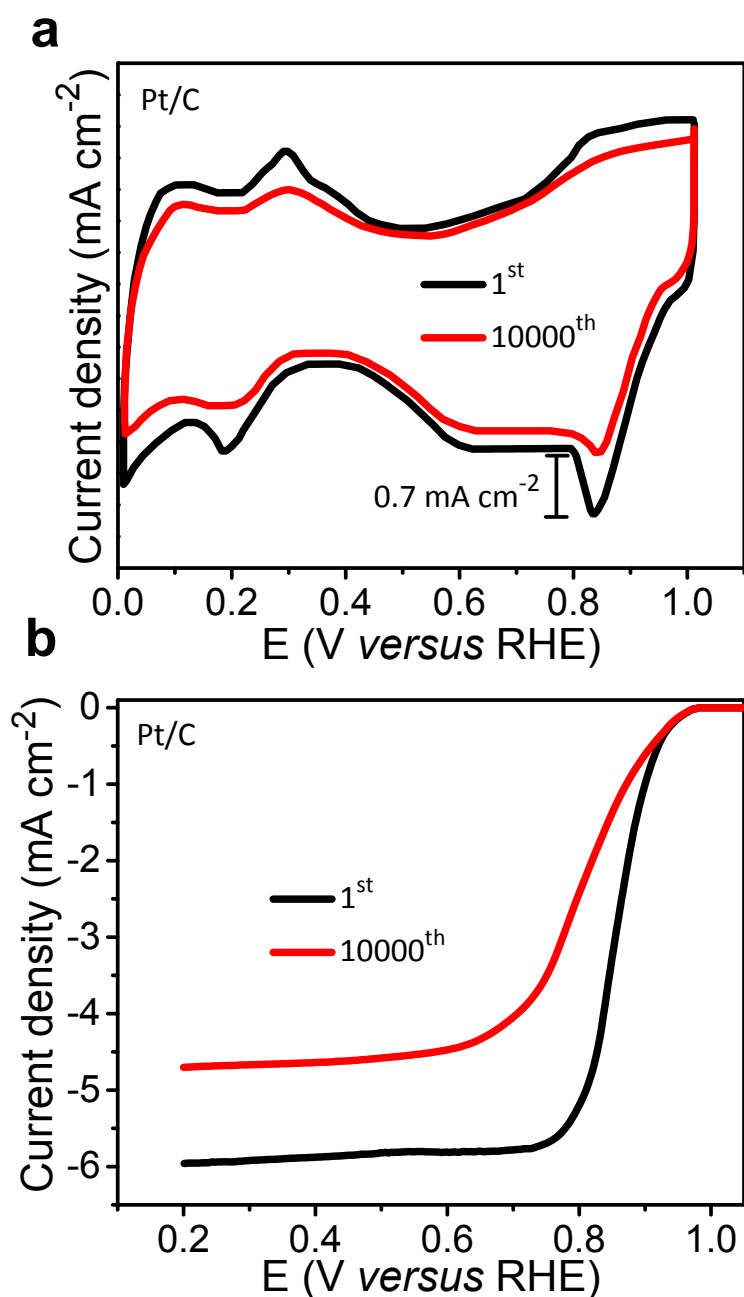


**Figure S16.** Accelerated durability tests: (a) Cyclic voltammograms and (b) LSVs before and after the 10000 cycles for Pt/C, respectively.

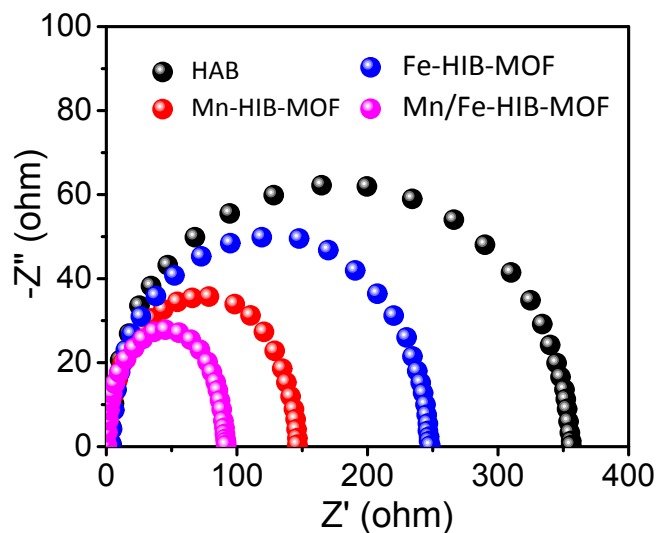


**Figure S17.** EIS spectra for M-HIB-MOFs for OER.

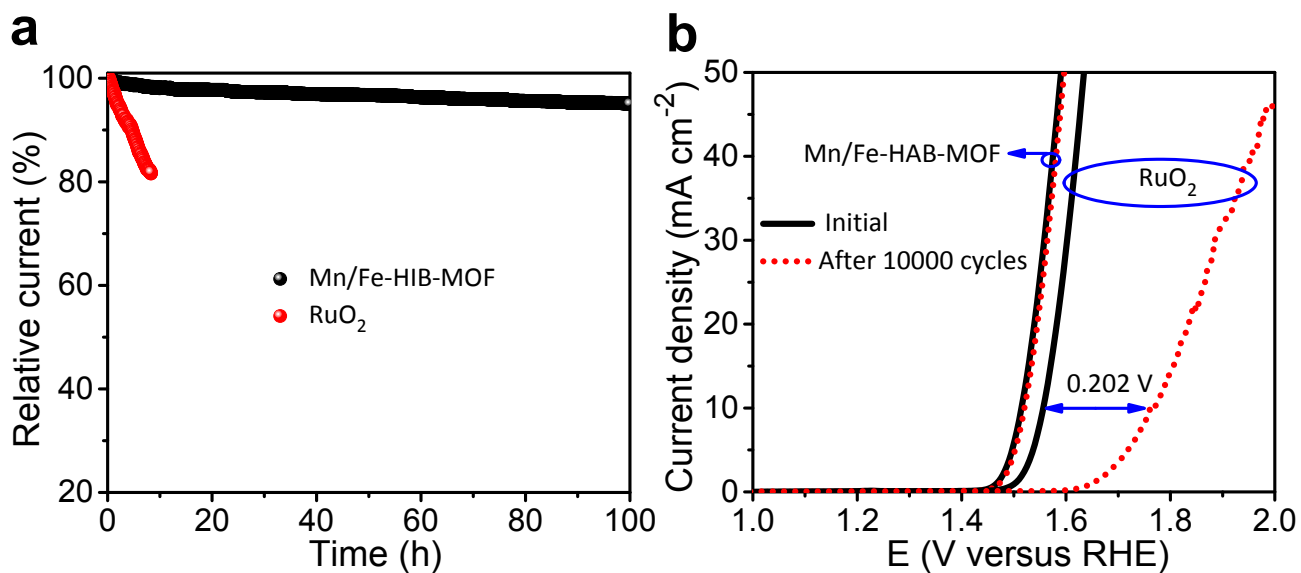


**Figure S18.** (a) OER  $I-t$  stability tests for Mn/Fe-HIB-MOF and RuO<sub>2</sub> for 1.51 V. (b) OER polarization profiles for Mn/Fe-HIB-MOF and RuO<sub>2</sub> before and after 10000 cycles. (Conditions: O<sub>2</sub> saturated KOH, 0.1 M)

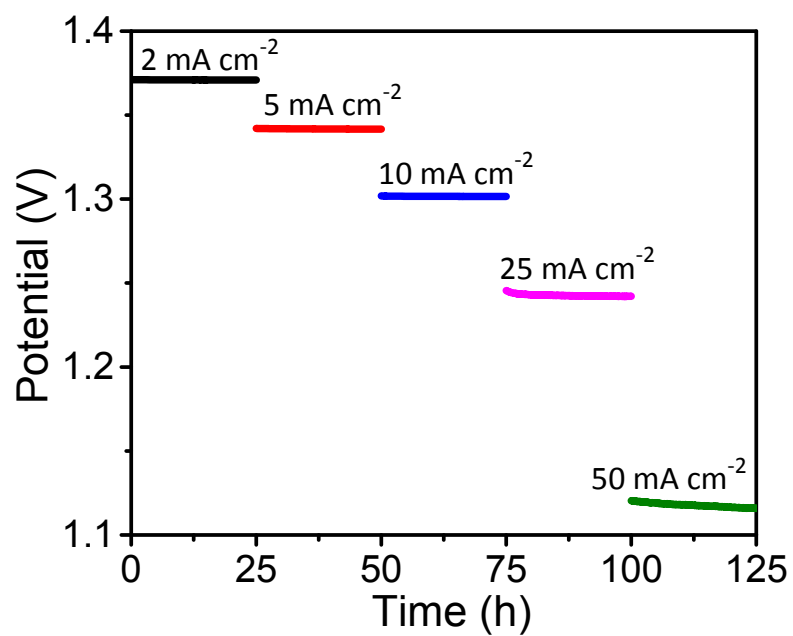


**Figure S19.** Galvanostatic discharge profiles for Mn/Fe-HIB-MOF for various current densities (2 to 50 mA cm<sup>-2</sup>).

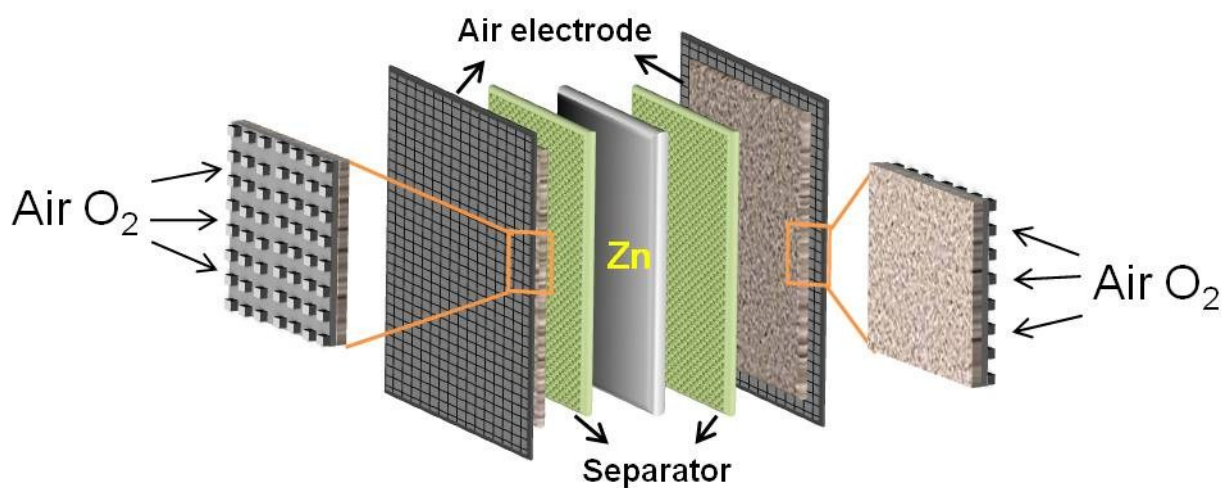


**Figure S20.** Schematic design of the fabricated rechargeable ZABs.

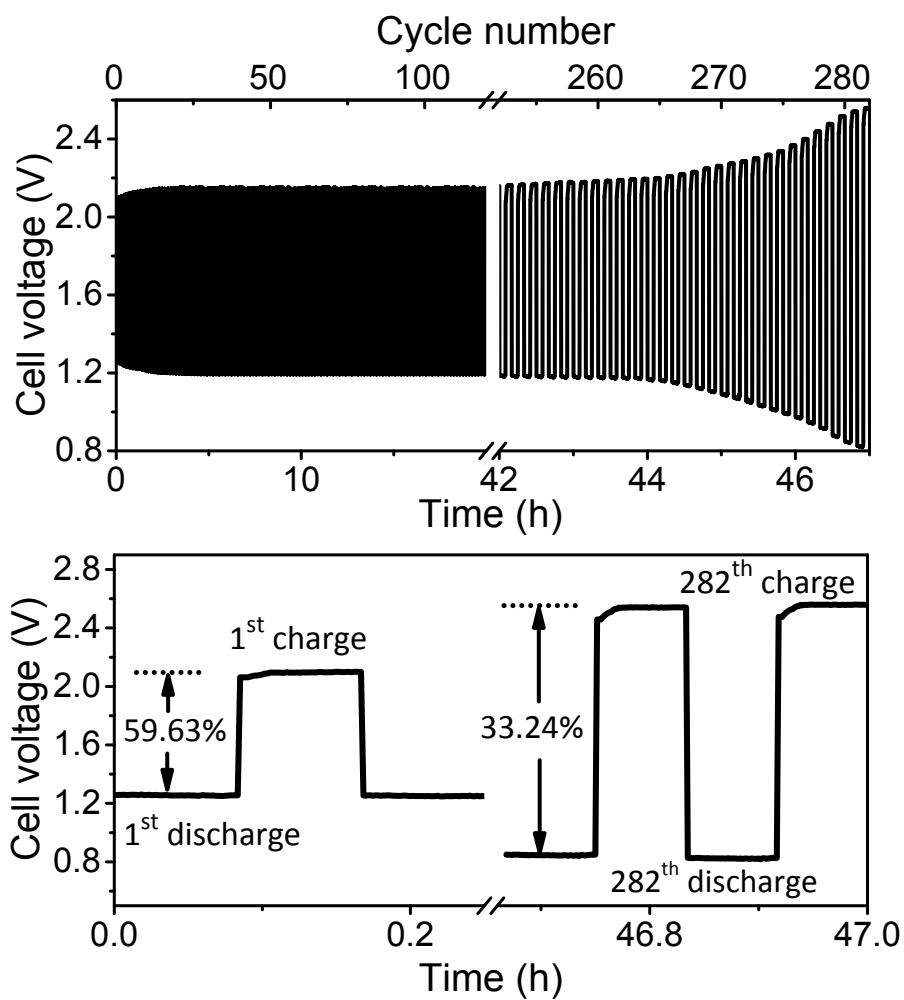


**Figure S21.** Discharging–charging pulse cycles for Pt/C + RuO<sub>2</sub> air cathodes. (Conditions: Current density = 10 mA cm<sup>-2</sup>, electrolyte = 6 M KOH)

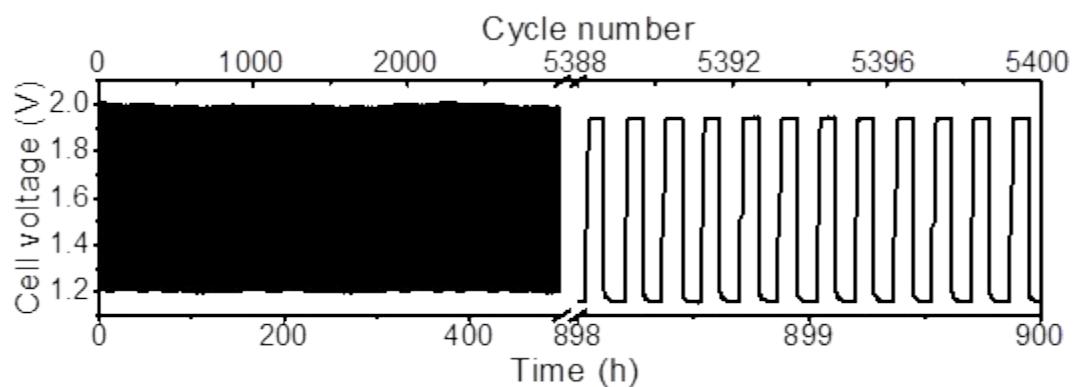


**Figure S22.** Long-life galvanostatic discharging–charging cycle performance with 20 mA  $\text{cm}^{-2}$ .

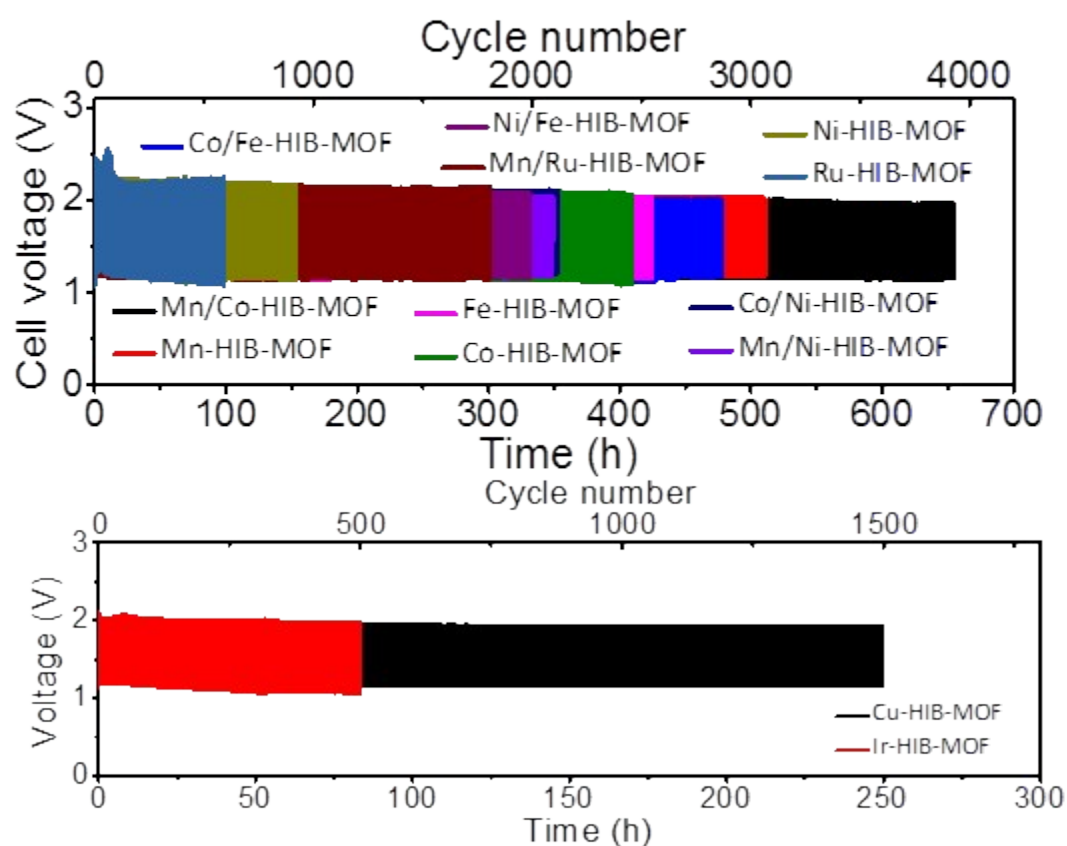


**Figure S23.** Long-life galvanostatic discharging–charging cycle performance for various mono and dual-linked HIB-MOFs at 10 mA  $\text{cm}^{-2}$ .

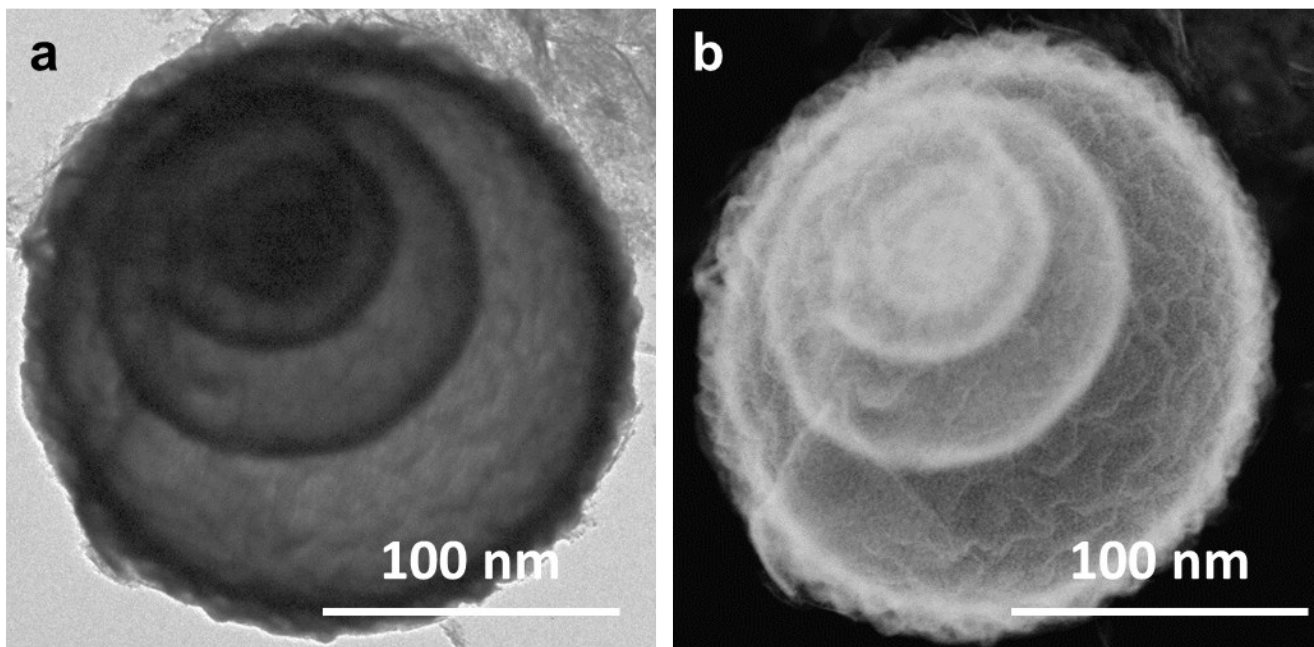


**Figure S24.** (a, b) STEM and HAADF images of the Mn/Fe-HIB-MOF over 6000 galvanostatic discharging–charging cycles.

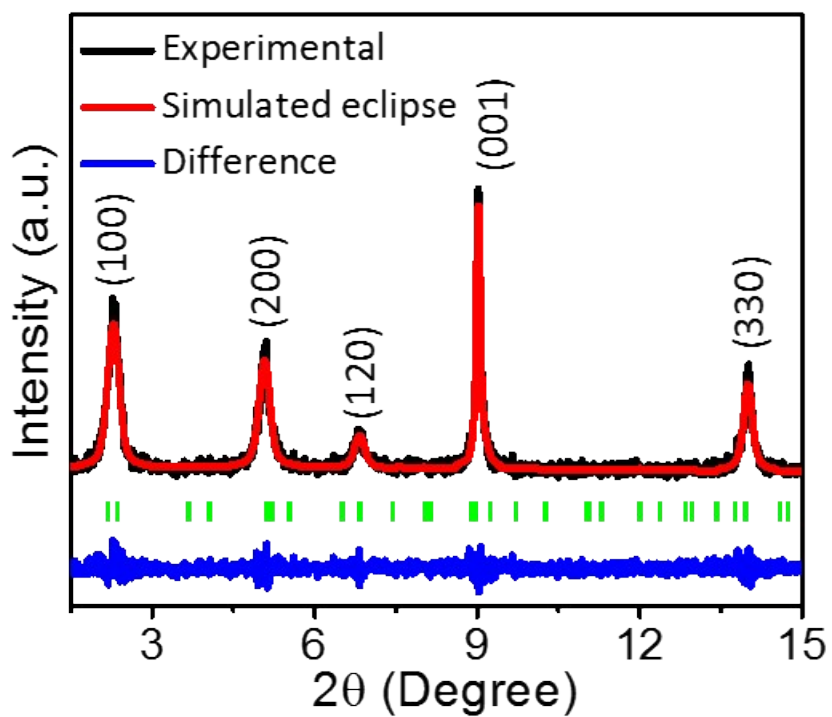


**Figure S25.** Pawley fitting of the powder XRD patterns of Mn/Fe-HIB-MOF after 6000 galvanostatic discharging–charging cycles. It retains their original crystal structure.

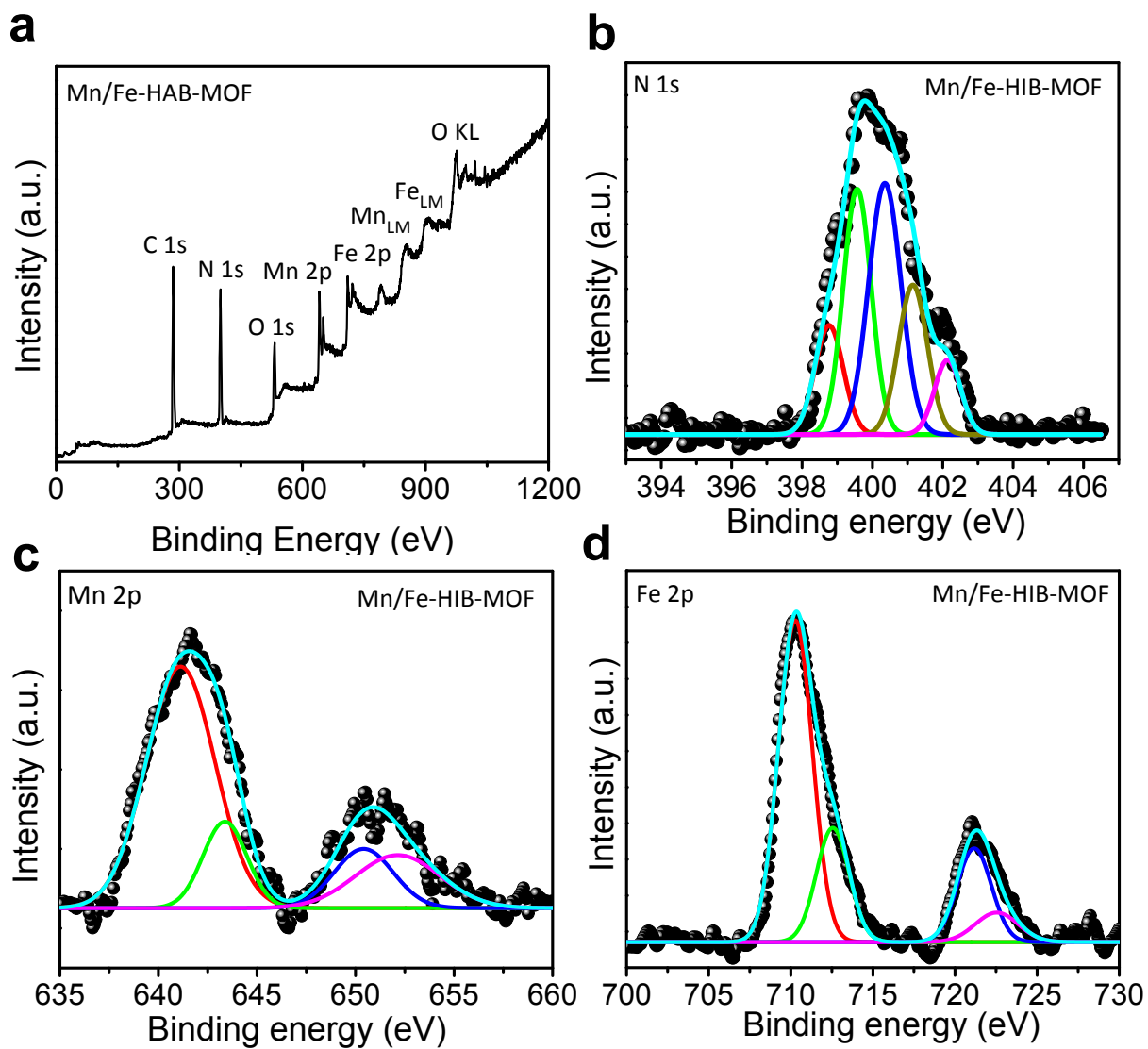


**Figure S26.** XPS spectra of Mn/Fe-HIB-MOF catalysts after 6000 galvanostatic discharging–charging cycles (a) survey, (b) N 1s, (c) Mn 2p, and (d) Fe 2p.

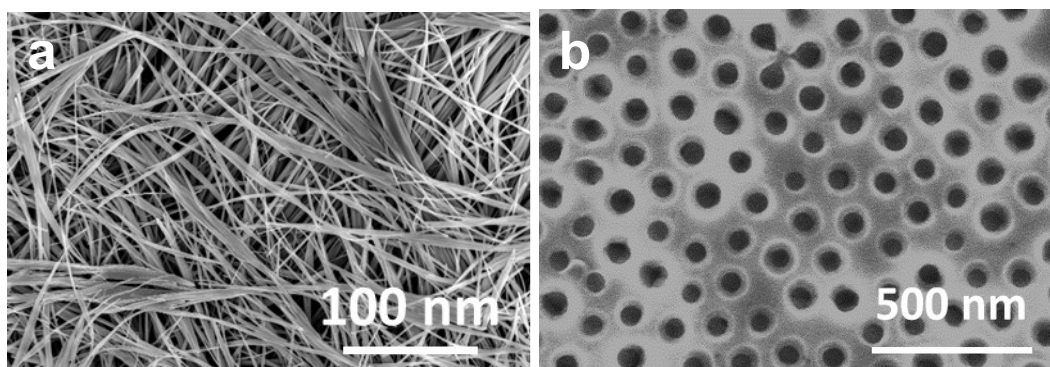


**Figure S27.** Microscopic images of the utilized electrolyte and anode for prepared solid-state Zn-air batteries. (a) Functionalized biological cellulose membrane and (b) chemically nano-engineered Zn foil.

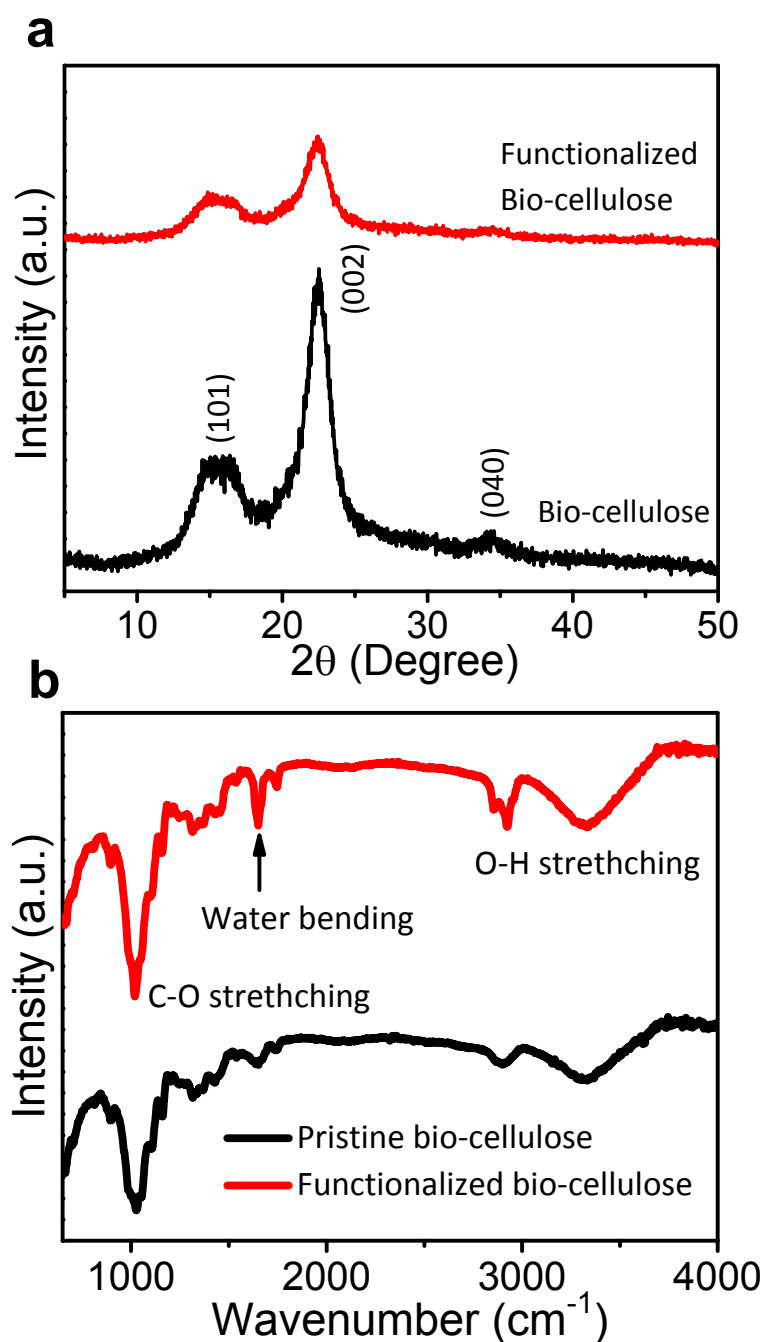


**Figure S28.** Structural analysis of the pristine and functionalized bio-cellulose membrane electrolyte: (a) X-ray diffraction patterns. (b) FTIR spectra.

Pristine bio-cellulose showed the characteristic peaks of crystalline cellulose I with (101), (10-1), (002), and (040) orientations (Figure S28a). Functionalized bio-cellulose membrane showed a strong decrement in the intensity of the characteristic peaks. The FBN membranes displayed the nanofibrils bundles and a pronounced decrease in (002) Bragg reflection from XRD measurements, implying the significant transformation of crystalline cellulose to amorphous phase. The enhancement of the amorphous phase can significantly improve the

flexibility of cellulose nanofibers and hydrophilic local domains adjacent to the hydroxide ions. This suggests the easiest ion transport through the hydrated regions in the prepared bio-cellulose electrolyte.<sup>S60</sup>

FTIR (S28b) displayed O-H stretching vibrations of intermolecular and intramolecular hydrogen bonds in the pristine bio-cellulose membranes, whereas the slight peak broadening in the functionalized bio-cellulose membrane. This illustrates that a large amount of water is absorbed in the amorphous domains. Furthermore, the strong water bending vibration in the amorphous regions observed at  $1650\text{ cm}^{-1}$  in the functionalized membranes, compared to the pristine membrane, imply the existence of a large amount of bound water. Additionally, the stretching vibrations observed in the range of  $1000\text{--}1300\text{ cm}^{-1}$  are corresponded to the functional groups of C-O, C=O, COOH,  $\text{-CH}_3$ , and C-H. The enhancement in the intensity of C-O/C=O stretching vibration with functionalization, illustrates the effective functionalization of bio-cellulose nanofibers.

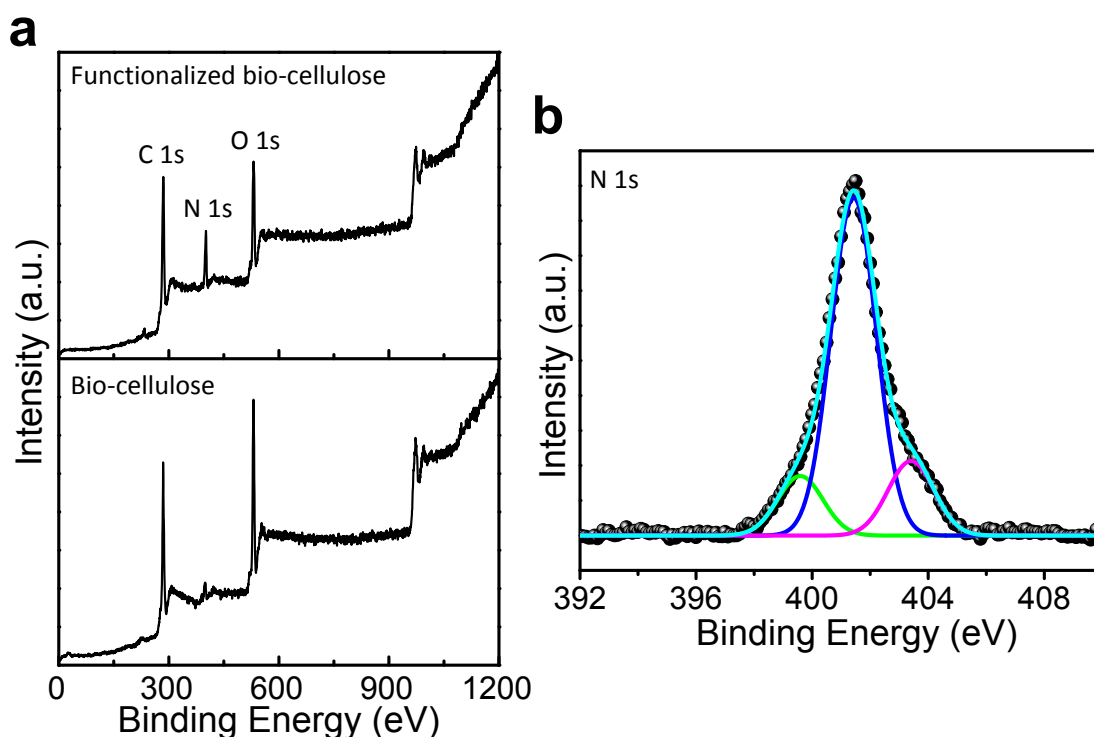


**Figure S29.** (a) XPS survey spectra of pristine and functionalized bio-cellulose membrane. (b) High resolution XPS spectrum of N 1s for functionalized bio-cellulose membrane.

The chemical functionalization of bio-cellulose membrane was investigated by using XPS analysis. XPS survey spectra displayed the decrease of O/C ratio from pristine bio-cellulose to functionalized bio-cellulose membrane (i.e., 1.30 to 1.02). This indicates an enhancement in the carbon atoms because of functionalized alkyl chains of choline. Pristine bio-cellulose

membrane showed small peak of nitrogen originated from chitosan groups. Moreover, the functionalized bio-cellulose membrane displayed significantly distinctive nitrogen peak at 401.4 eV, which was assigned to quaternary nitrogen species. The weak peak of quaternary  $N^+-O^-$  species was also observed at 403.4 eV. This result clearly demonstrates the existence of quaternary ammonium as prevailing moieties.

Functionalized bio-cellulose membranes showed excellent ion conductivity of ( $64 \text{ mS cm}^{-1}$ ) compared to those of commercial A201 ( $40 \text{ mS cm}^{-1}$ ) and pristine bio-cellulose membranes ( $12 \text{ mS cm}^{-1}$ ). This suggests the dissociation of functional groups in the hydrated regions and trapping of superfluous alkali during hydroxide exchange process because of nanoporous structure of the bio-cellulose membranes, leading to an enhancement in the ion conductivity. The functionalized bio-cellulose membrane showed a comparable linear trend in positive temperature conductivity with commercial A201 membrane, implying the Grotthuss hopping mechanism dominates the transport of hydroxide ions ( $OH^-$ ). The calculated activation energy of functionalized membrane ( $2.99 \text{ kJ mol}^{-1}$ ) is significantly smaller compared to A201 ( $17.11 \text{ kJ mol}^{-1}$ ), illustrating hydroxide ion hopping in polymeric chains. These results confirm the remarkable amount of free volume in the functionalized membrane with excellent segmental motions of celluloses in the amorphous region. The determined ion transfer numbers of the  $K^+$ ,  $Zn^{2+}$ ,  $OH^-$ , and  $CH_3COO^-$  ions are 0.245, 0.0125, 0.734, and 0.009, illustrates the fast ion transport of  $OH^-$  (Figure S22).

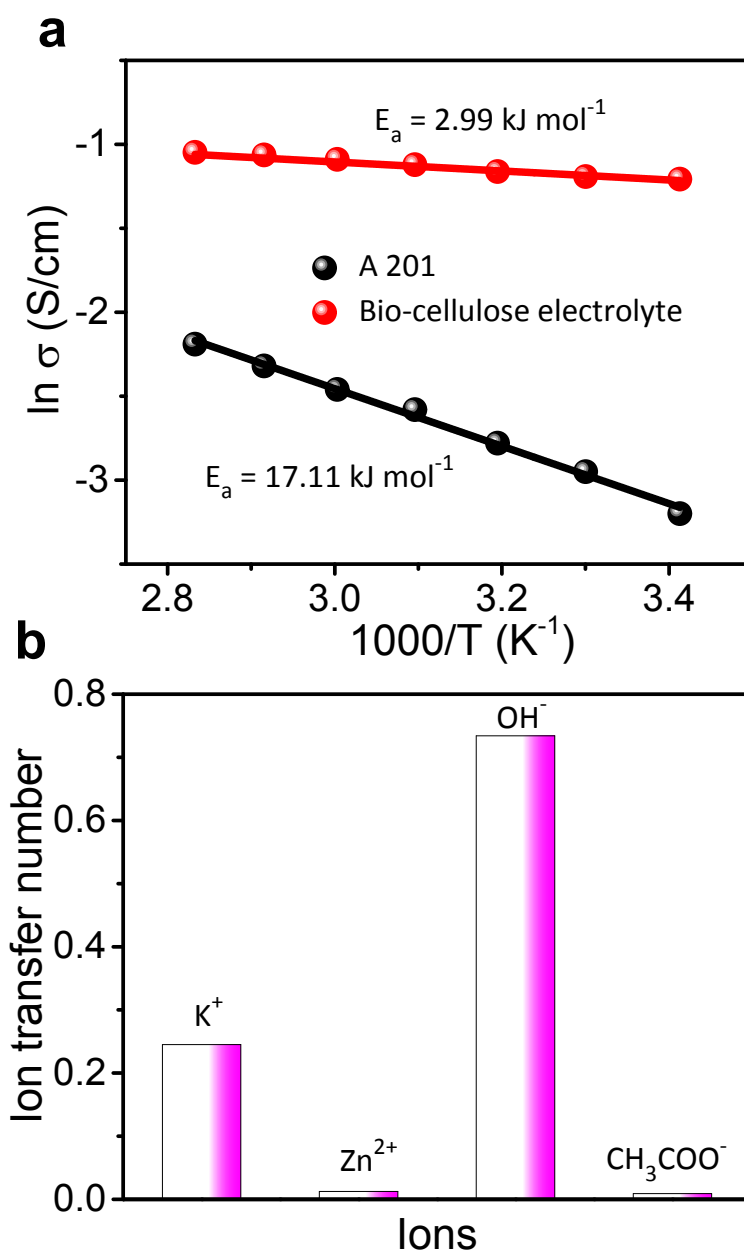


**Figure S30.** (a) Arrhenius plots for the ion conductivity of the functionalized bio-cellulose and A 201 membrane. (b) Ion transfer number in the functionalized cellulose membrane.

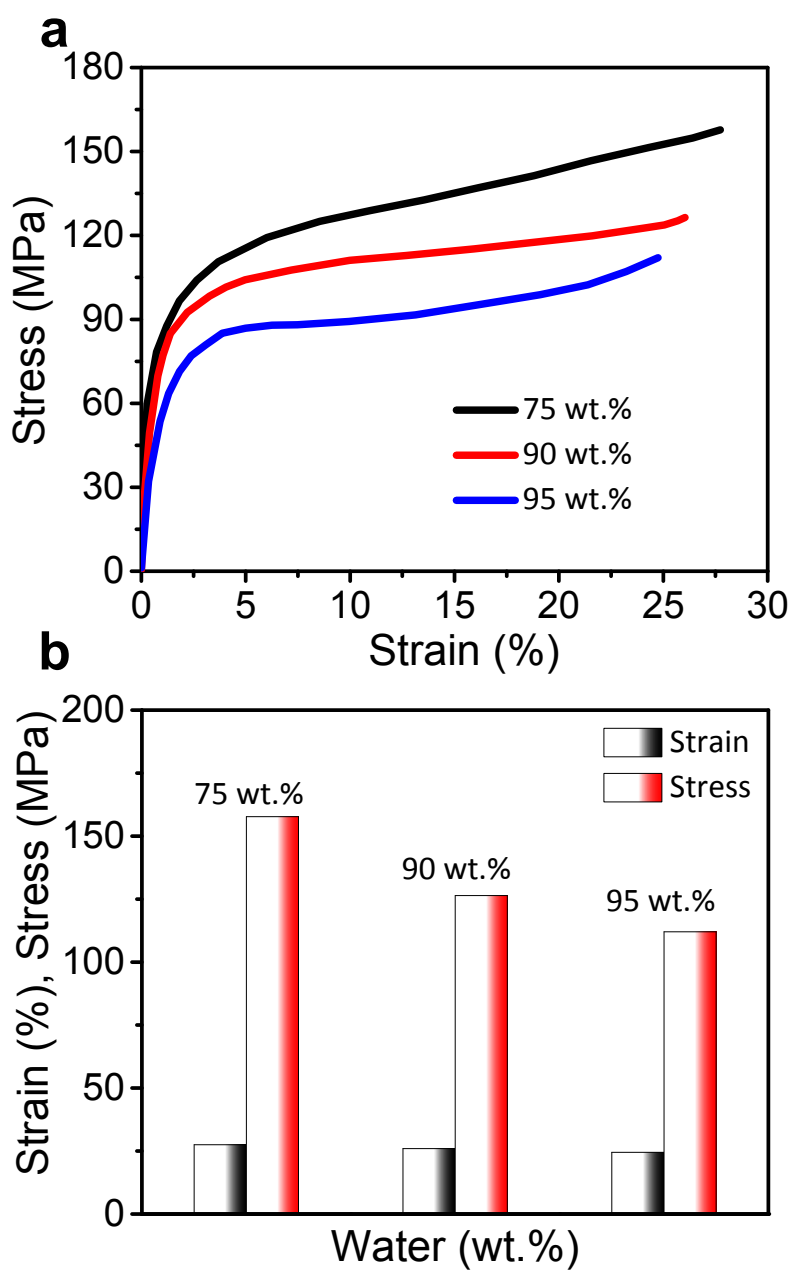


**Figure S31.** Mechanical properties of the functionalized bio-cellulose membrane with different absorbed water contents. (a) Stress–strain curves. (b) Maximum strength and strain.

Both the stress and strain were reduced with enhanced amount of absorbed solution, showing low-tolerance stress and strain. It retains 112 MPa and 24% of stress and strain even after 95 wt.% absorbing solution, confirms the outstanding mechanical properties.

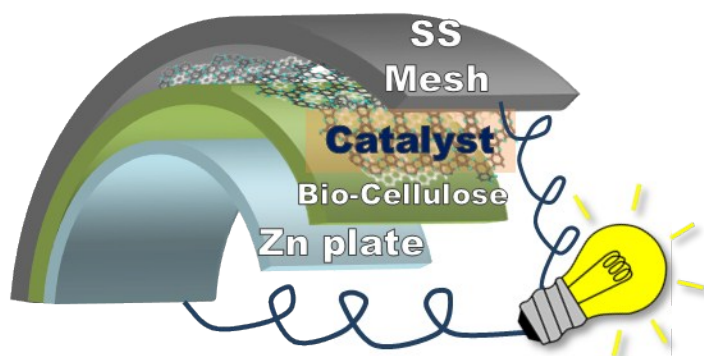


**Figure S32.** Schematic illustration of the rechargeable all-solid-state Zn–air battery.

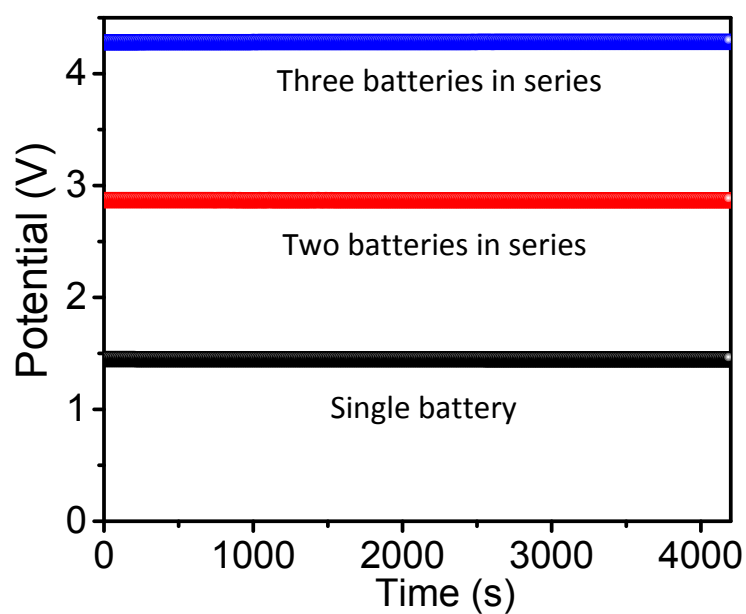


**Figure S33.** Open-circuit potentials (OCPs) for the fabricated single Zn–air battery, series connected two and three batteries.

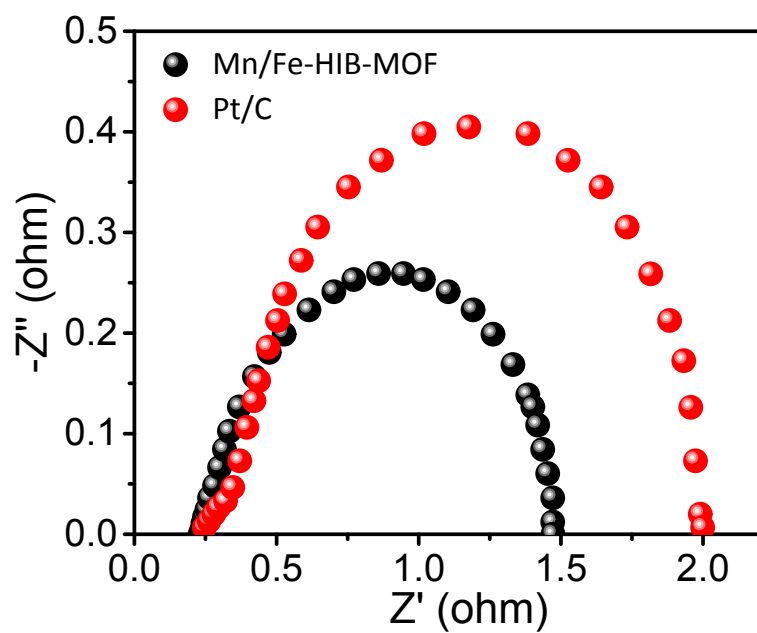


**Figure S34.** Electrochemical impedance spectra of tandem ZABs with Mn/Fe-HIB-MOF and Pt/C electrodes at a potential of 1.0 V.

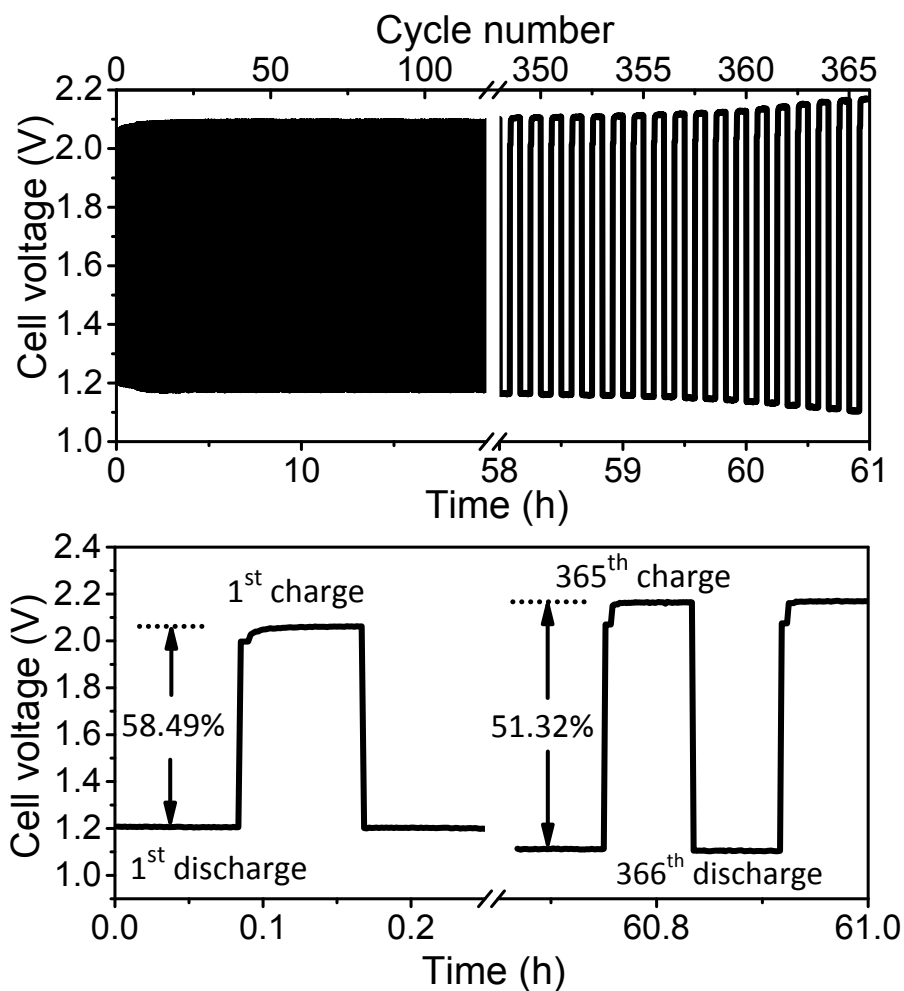


**Figure S35.** Galvanostatic discharging–charging profiles of solid-state rechargeable ZAB with Pt/C+RuO<sub>2</sub> as the air cathodes (Electrolyte- functionalized bio-cellulose electrolyte).

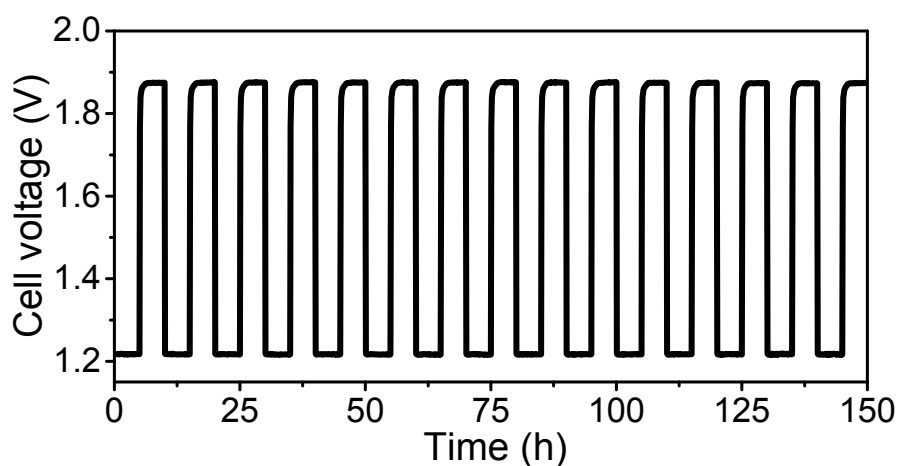


**Figure S36.** Galvanostatic pulse cycling for solid-state flexible ZABs at 25 mA cm<sup>-2</sup> with duration of 10 h per cycle.

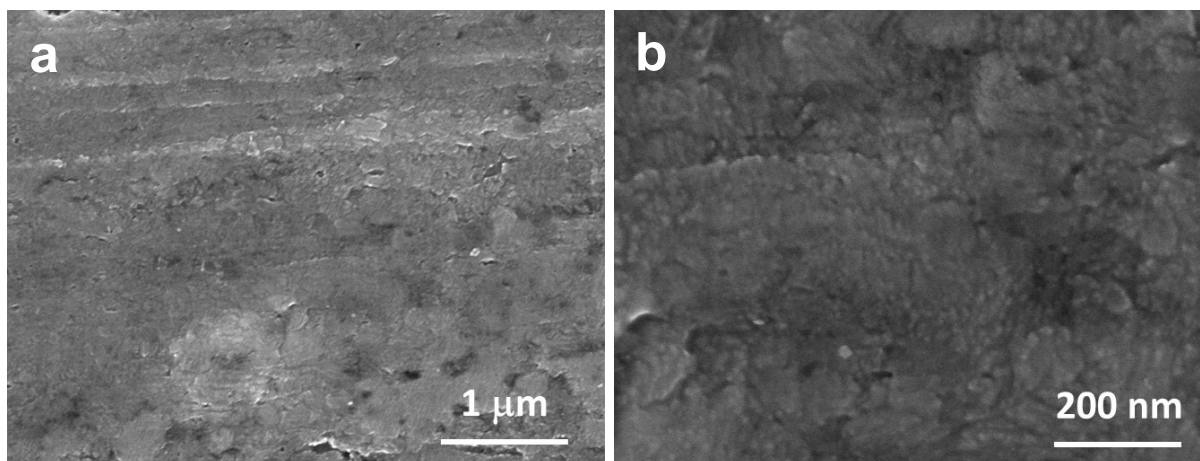


**Figure S37.** (a, b) SEM images of the Zn electrode after continuous discharge/charge cycle performance. This clearly confirms the absence of dendrites formation on the Zn electrode after discharge/charge cycling.

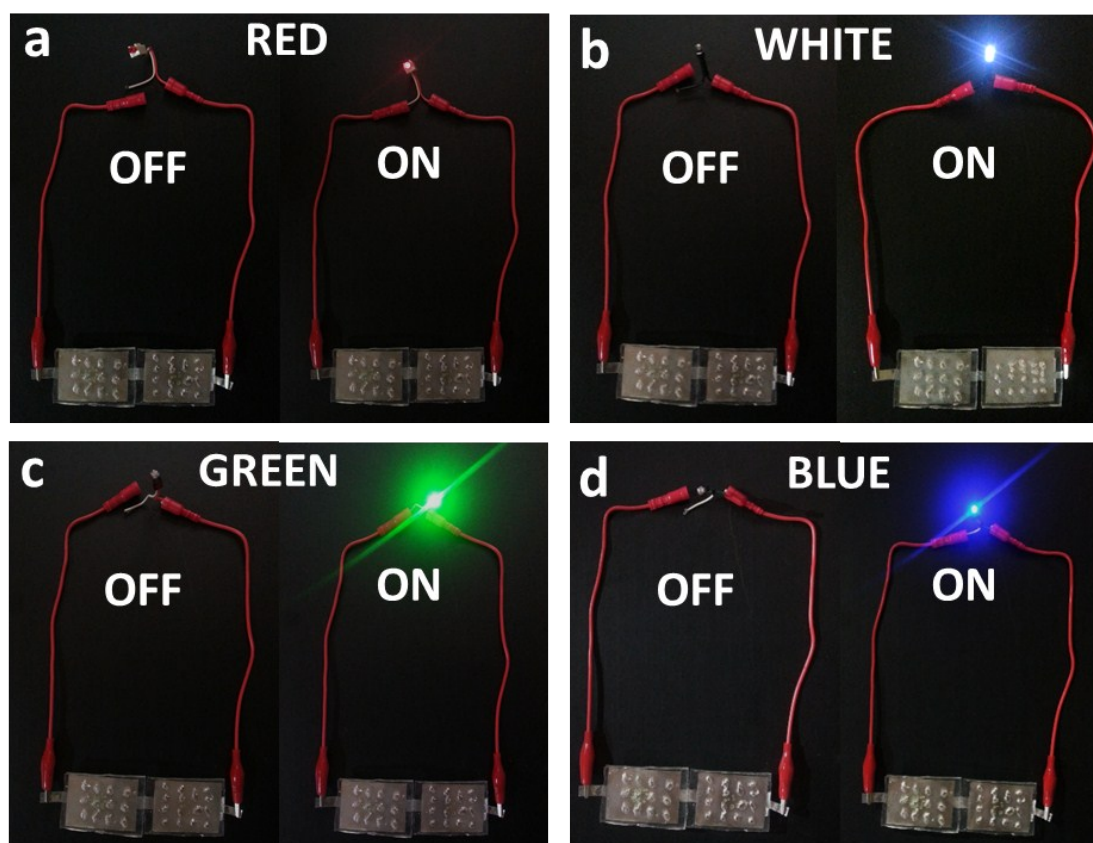


**Figure S38.** Optical images of LEDs before and after powering by two ZABs in series (a) RED LED, (b) WHITE LED, (c) GREEN LED, and (d) BLUE LED.

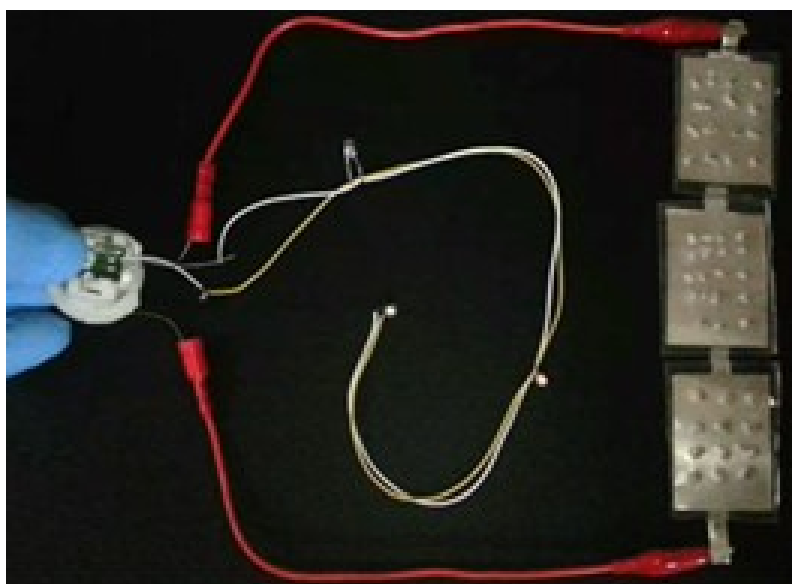


**Figure S39.** Optical image of backside of demonstration of powering LEDs.

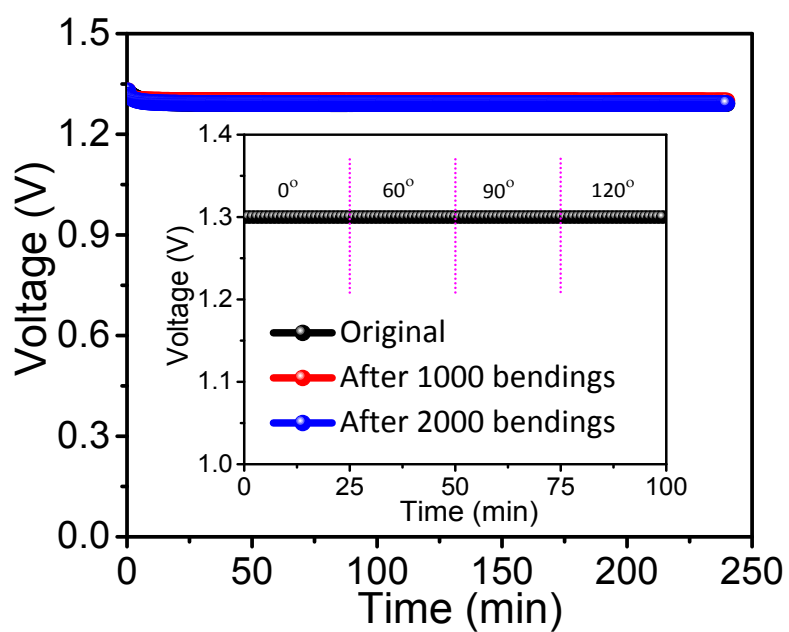


**Figure S40.** Discharge voltage profiles for the flexible ZABs at  $10 \text{ mA cm}^{-2}$  with bending times. Inset shows discharge voltages for  $0^\circ$ ,  $60^\circ$ ,  $90^\circ$ , and  $120^\circ$  bending angles.

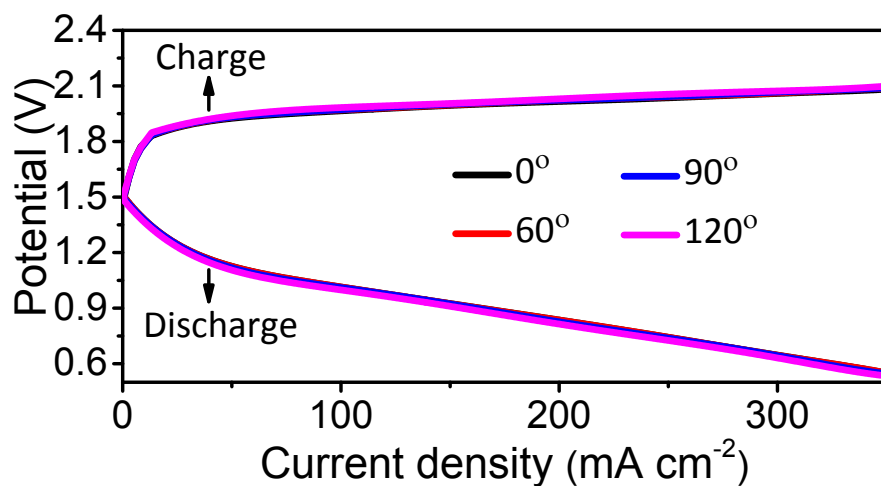


**Figure S41.** Voltage–current polarization data for the flexible ZABs at  $10 \text{ mA cm}^{-2}$  based on different bending states.

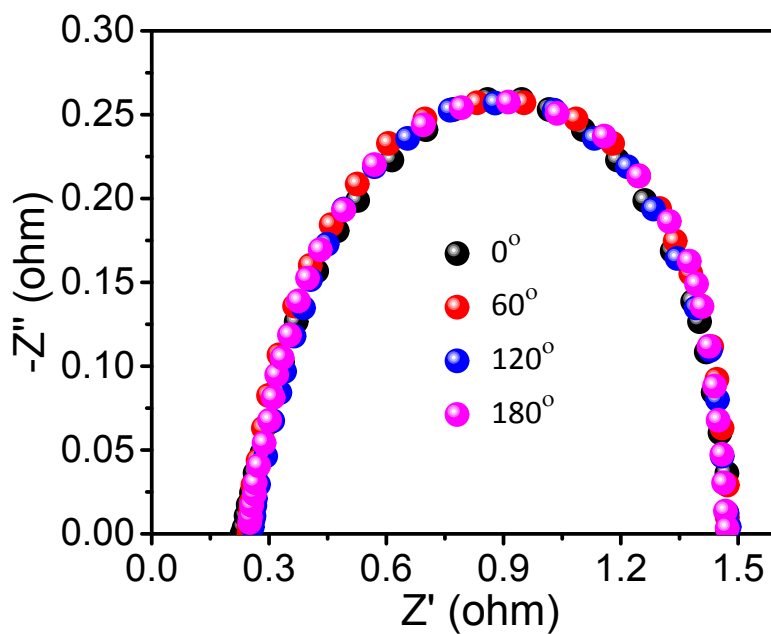


**Figure S42.** EIS for the flexible tandem ZAB cells with different bending states at  $10 \text{ mA cm}^{-2}$ .

## Supplementary Tables

**Table S1.** Crystallographic analysis, conditions of PXRD, and Pawley fitting results of Mn-HIB-MOF, Fe-HIB-MOF, and Mn/Fe-HIB-MOF catalysts.

Parameters	Catalysts		
	MnC <sub>4</sub> N <sub>4</sub> H <sub>4</sub>	FeC <sub>4</sub> N <sub>4</sub> H <sub>4</sub>	Mn/FeC <sub>4</sub> N <sub>4</sub> H <sub>4</sub>
Chemical formula	MnC <sub>4</sub> N <sub>4</sub> H <sub>4</sub>	FeC <sub>4</sub> N <sub>4</sub> H <sub>4</sub>	Mn/FeC <sub>4</sub> N <sub>4</sub> H <sub>4</sub>
Molecular weight	162.9	163.8	163.4
Crystal structure	Hexagonal	Hexagonal	Hexagonal
Space group	P6/mmm	P6/mmm	P6/mmm
a (Å)	13.2836 (2)	13.3025 (2)	13.2467(2)
c (Å)	3.1422 (1)	3.1826 (1)	3.1589 (1)
Z	3	3	3
Temperature (K)	300	300	300
Wavelength (Å)	0.45336	0.45336	0.45336
2θ range (°)	1.6–15	1.6–15	1.6–15
R <sub>p</sub>	0.0325	0.0359	0.0417
R <sub>wp</sub>	0.0402	0.0436	0.0512
R <sub>exp</sub>	0.0133	0.0119	0.0165
GOF	3.0225	3.663	3.103

**Table S2.** Quantitative elemental analysis of Mn-HIB-MOF, Fe-HIB-MOF, and Mn/Fe-HIB-MOF catalysts.

Sample	C (%)	N (%)	Mn (%)	Fe (%)
Mn-HIB-MOF	27.76	32.21	35.47	-
Fe-HIB-MOF	28.2	32.10	-	35.19
Mn/Fe-HIB-MOF	27.92	32.43	17.59	17.35

**Table S3.** Quantitate distribution of nitrogen species: pyridinic (N1), pyrrolic or metal-coordinated N (N2), graphitic (N3), quaternary (N4), and oxidized N (N5) for the HAB, Mn-HIB-MOF, Fe-HIB-MOF, and Mn/Fe-HIB-MOF catalysts.

Sample	N1 (%)	N2 (%)	N3 (%)	N4 (%)	N5 (%)
HAB	398.50	399.94	-	401.12	402.31
Mn-HIB-MOF	398.39	399.54	400.41	401.42	402.22
Fe-HIB-MOF	398.72	399.59	400.43	401.52	402.41
Mn/Fe-HIB-MOF	398.60	399.41	400.35	401.07	402.02

**Table S4.** Summary of the bifunctional ORR and OER performance for previously reported excellent catalysts.

Catalyst	Loading (mg cm <sup>-2</sup> )	ORR onset potential (V vs. RHE)	ORR Tafel slope (mV dec <sup>-1</sup> )	ORR half-wave potential (E <sub>1/2</sub> ) (V vs. RHE)	OER onset potential (V vs. RHE)	OER Tafel slope (mV dec <sup>-1</sup> )	OER potential @ 10 mA cm <sup>-2</sup> (E <sub>j=10</sub> ) (V vs. RHE)	Overall oxygen electrode activity $\Delta E$ (E <sub>j=10</sub> - E <sub>1/2</sub> ) (V)	References
Mn/Fe-HIB-MOF	0.15	0.98	36	0.883	1.33	45	1.51	0.627	This work
Mn/Co-HIB-MOF	0.15	0.97	-	0.85	1.46	-	1.63	0.78	This work
Mn/Ni-HIB-MOF	0.15	0.94	-	0.81	1.40	-	1.62	0.81	This work
Mn/Ru-HIB-MOF	0.15	0.92	-	0.78	1.43	-	1.61	0.83	This work
NPMC-1000	0.10	0.94	-	0.85	1.30	-	-	-	S10
NiO/CoN PINWs	0.20	0.89	35	0.68	1.53	-	1.53	0.85	S11
PS-CNS	0.15	0.97	61	0.87	1.26	64	1.56	0.69	S12
Co <sub>4</sub> N/CNW/CC	0.20	0.89	-	0.80	1.50	81	1.54	0.74	S13
CCO@C	0.2	0.95	-	0.86	1.47	74	1.56	0.70	S14
1100-CNS	0.42	0.99	58	0.88	1.50	292	1.69	0.81	S15
C-MOF-C2-900	0.5	0.92	-	0.817	1.50	79	1.58	0.763	S16
Co-N <sub>2</sub> B-CSs	0.1	0.89	64	0.83	1.42	-	1.66	0.83	S17
S-C <sub>2</sub> NA	0.15	0.98	54	0.88	1.28	62	1.53	0.65	S18
FeN <sub>x</sub> -PNC	0.14	0.99	-	0.86	1.56	80	1.63	0.77	S19

CFZr(0.3)/N-rGO	0.3	0.85	-	0.76	1.4	-	1.6	0.84	S20
NDGs-800	0.2	0.98	81	0.85	1.5	132	1.68	0.83	S21
CMO/S-300	0.3	0.915	52	0.76	1.5	-	1.70	0.94	S22
Co/Co <sub>3</sub> O <sub>4</sub> @PGS	0.3	0.97	52.6	0.89	1.52	76.1	1.58	0.69	S23
DN-CP@G	0.2	0.95	-	0.801	1.5	65	1.788	0.987	S24
N-GRW	0.30	0.92	53	0.84	1.53	47	1.59	0.75	S25
NCNF-1000	0.10	0.94		0.85	1.30		1.84	1.02	S26
NiCo <sub>2</sub> S <sub>4</sub> /N-CNT	0.25	0.93	-	0.80	-	-	1.60	0.80	S27
NC-Co <sub>3</sub> O <sub>4</sub> -90	1.2	0.91	-	0.87	-	-	1.59	0.72	S28
FeNi@N-GR	0.2	0.94	-	0.83	1.38	62	1.44	0.61	S29
PS-CNF	0.2	0.95	29	0.86	1.32	89	1.55	0.69	S30
S,N-Fe/N/C-CNT	0.25	0.94	-	0.84	1.45	82	1.60	0.76	S31
Co <sub>3</sub> O <sub>4</sub> /NPGC	0.20	0.97	-	0.84	1.45	-	1.68	0.84	S32
PCN-CFP	0.20	0.94	122.3	0.67	1.53	61.6	1.63	0.96	S33
N-GCNT/FeCo-3	0.40	1.03	66.8	0.92	1.42	99.5	1.73	0.81	S34
CoO/N-G	0.70	0.90	48	0.81	1.30	71	1.57	0.76	S35
S-GNS/NiCo <sub>2</sub> S <sub>4</sub>	0.3	0.93	-	0.88	1.48	65	1.56	0.69	S36

**Table S5.** State of the art of primary Zn–air batteries in alkaline electrolytes for various electrocatalysts.

Catalyst	OCP (V)	Power density (mW cm <sup>-2</sup> )	Specific capacity (mA h g <sup>-1</sup> )	Durability (h)	References
Mn/Fe-HIB-MOFs	1.50	195	768	-	This work
NPMC-1000	1.48	55	735	240 (~1.3 V)	S10
NiO/CoN PINWs	1.46	79.6	690	-	S11
P,S-CNS	1.51	198	830	210 (~1.3 V)	S12
Co <sub>4</sub> N/CNW/CC	1.40	174	774	-	S13
1100-CNS	1.49	151	-	100 (~ 1.3 V)	S15
C-MOF-C2-900	1.43	105	768	-	S16
Co-N <sub>3</sub> B-CSs	1.43	100.4	-	-	S17
S-C <sub>2</sub> NA	1.49	209	863	-	S18
FeN <sub>x</sub> -PNC	1.55	278	-	-	S19
CFZr(0.3)/N-rGO	1.39	-	732	-	S20
NDGs-800	1.45	115.2	750.8	-	S21
CMO/S-300	1.5	152	-	-	S22
Co/Co <sub>3</sub> O <sub>4</sub> @PGS	1.45	118.27	-	-	S23
DN-CP@G	1.43	135	591	-	S24
N-GRW	1.46	65	873	-	S25
NCNF-1000	1.48	185	660	-	S26
NC-Co <sub>3</sub> O <sub>4</sub> -90	1.44	-	-	-	S28
FeNi@N-GR	1.48	85	765	-	S29
PS-CNF	1.49	231	698	240 (~1.3 V)	S30
S-GNS/NiCo <sub>2</sub> S <sub>4</sub>	1.38	216.3	-	-	S36
CNT@POF	1.49	237	772.7	-	S37
PbMnO <sub>x</sub>	-	40	-	50 (~1.2 V)	S38
N <sub>3</sub> B-CNT	-	25	-	30 (~1.1 V)	S39
NiC <sub>2</sub> O <sub>4</sub>	-	-	580	10 (~1.25 V)	S40
FePc-Py-CNTs	-	-	-	100 (~1.2 V)	S41
CoO/N-CNT	1.40	265	570	-	S42
CuPt-NC	1.50	250	560	-	S43
MnO <sub>x</sub> /C	1.40	190	290	-	S44
CuS/NiS <sub>2</sub>	1.44	172.4	775	-	S45

**Table S6.** Summary of state-of-the-art rechargeable Zn–air batteries in alkaline environments.

Catalyst	Recharge ability	Reference
Mn/Fe-HIB-MOFs	600 s/cycle for 6000 cycles; 1000 h@10 mA cm <sup>-2</sup>	This work
Mn/Fe-HIB-MOFs	600 s/cycle for 5400 cycles; 900 h@20 mA cm <sup>-2</sup>	This work
Mn/Co-HIB-MOFs	600 s/cycle for 3900 cycles; 650 h@10 mA cm <sup>-2</sup>	This work
Mn/Ni-HIB-MOFs	600 s/cycle for 2100 cycles; 350 h@10 mA cm <sup>-2</sup>	This work
Mn/Ru-HIB-MOFs	600 s/cycle for 1800 cycles; 300 h@10 mA cm <sup>-2</sup>	This work
Co/Ni-HIB-MOFs	600 s/cycle for 2100 cycles; 350 h@10 mA cm <sup>-2</sup>	This work
Co/Fe-HIB-MOFs	600 s/cycle for 2700 cycles; 450 h@10 mA cm <sup>-2</sup>	This work
Ni/Fe-HIB-MOFs	600 s/cycle for 2000 cycles; 333.3 h@10 mA cm <sup>-2</sup>	This work
Mn-HIB-MOFs	600 s/cycle for 3000 cycles; 500 h@10 mA cm <sup>-2</sup>	This work
Fe-HIB-MOFs	600 s/cycle for 2580 cycles; 430 h@10 mA cm <sup>-2</sup>	This work
Co-HIB-MOFs	600 s/cycle for 2400 cycles; 400 h@10 mA cm <sup>-2</sup>	This work
Ni-HIB-MOFs	600 s/cycle for 900 cycles; 150 h@10 mA cm <sup>-2</sup>	This work
Cu-HIB-MOFs	600 s/cycle for 1500 cycles; 250 h@10 mA cm <sup>-2</sup>	This work
Ru-HIB-MOFs	600 s/cycle for 600 cycles; 100 h@10 mA cm <sup>-2</sup>	This work
Ir-HIB-MOFs	600 s/cycle for 500 cycles; 83.3 h@10 mA cm <sup>-2</sup>	This work
NPMC-1000	600 s/cycle for 600 cycles; 100 h@2 mA cm <sup>-2</sup>	S10
NiO/CoN PINWs	600 s/cycle for 25 cycles; 8.3 h@50 mA cm <sup>-2</sup>	S11
P,S-CNS	720 s/cycle for 500 cycles; 100 h@2 mA cm <sup>-2</sup>	S12
Co <sub>4</sub> N/CNW/CC	1200 s/cycle for 408 cycles; 136 h@10 mA cm <sup>-2</sup>	S13
CCO@C	1800 s/cycle for 160 cycles; 80 h @2 mA cm <sup>-2</sup>	S14
1100-CNS	660 s/cycle for 300 cycles; 55 h @10 mA cm <sup>-2</sup>	S15
C-MOF-C2-900	1200 s/cycle for 360 cycles; 120 h @2 mA cm <sup>-2</sup>	S16
Co-N,B-CSs	394 s/cycle for 128 cycles; 14 h @5 mA cm <sup>-2</sup>	S17
S-C <sub>2</sub> NA	2 h/cycle for 375 cycles; 750 h@10 mA cm <sup>-2</sup>	S18
FeN <sub>x</sub> -PNC	660 s/cycle for 220 cycles; 40 h @5 mA cm <sup>-2</sup>	S19
CFZr(0.3)/N-rGO	3600 s/cycle for 11 cycles; 11 h @15 mA cm <sup>-2</sup>	S20
NDGs-800	1200 s/cycle for 234 cycles; 78 h @10 mA cm <sup>-2</sup>	S21

CMO/S-300	400 s/cycle for 120 cycles; 13 h @5 mA cm <sup>-2</sup>	S22
Co/Co <sub>3</sub> O <sub>4</sub> @PGS	600 s/cycle for 4800 cycles; 800 h @10 mA cm <sup>-2</sup>	S23
DN-CP@G	3600 s/cycle for 250 cycles; 250 h @5 mA cm <sup>-2</sup>	S24
N-GRW	1h/cycle for 160 cycles; 160 h@2 mA cm <sup>-2</sup>	S25
NCNF-1000	600 s/cycle for 500 cycles; 83 h@10 mA cm <sup>-2</sup>	S26
NiCo <sub>2</sub> S <sub>4</sub> /N-CNT	400 s/cycle for 150 cycles; 17 h@10 mA cm <sup>-2</sup>	S27
NC-Co <sub>3</sub> O <sub>4</sub> -90	1200 s/cycle for 600 cycles; 200 h@10 mA cm <sup>-2</sup>	S28
FeNi@N-GR	1200 s/cycle for 120 cycles; 40 h @20 mA cm <sup>-2</sup>	S29
PS-CNF	700 s/cycle for 600 cycles; 120 h @2 mA cm <sup>-2</sup>	S30
Co <sub>3</sub> O <sub>4</sub> /NPGC	1200 s/cycle for 250 cycles; 83 h@5 mA cm <sup>-2</sup>	S32
PCN-CFP	600 s/cycle for 50 cycles; 8.3 h@20 mA cm <sup>-2</sup>	S33
N-GCNT/FeCo-3	600 s/cycle for 240 cycles; 40 h@125 mA cm <sup>-2</sup>	S34
S-GNS/NiCo <sub>2</sub> S <sub>4</sub>	2400 s/cycle for 150 cycles; 100 h @10 mA cm <sup>-2</sup>	S36
CNT@POF	1200 s/cycle for 200 cycles; 67 h @2 mA cm <sup>-2</sup>	S37
CoO/N-CNT + NiFe LDH/Ni	10 h/cycle for 10 cycles; 200 h@20 mA cm <sup>-2</sup>	S42
CuS/NiS <sub>2</sub>	1800 s/cycle for 500 cycles; 83 h @25 mA cm <sup>-2</sup>	S45
macro/meso-NC-NH <sub>3</sub> + COMT@Ni	4 h/cycle for 200 cycles; 800 h@10 mA cm <sup>-2</sup>	S46
Co <sub>3</sub> O <sub>4</sub> NWs	600 s/cycle for 100 cycles; 17 h@50 mA cm <sup>-2</sup>	S47
NCNT/CoO-NiO-NiCo	600 s/cycle for 100 cycles; 17 h@20 mA cm <sup>-2</sup>	S48
LBSCFO-50	600 s/cycle for 100 cycles; 17 h@10 mA cm <sup>-2</sup>	S49
Ni <sub>6/7</sub> Fe <sub>1/7</sub> -OH-6/CNT	600 s/cycle for 150 cycles; 25 h@15 mA cm <sup>-2</sup>	S50
NiCo/PFC	2 h/cycle for 300 cycles; 600 h@10 mA cm <sup>-2</sup>	S51
Ni <sub>3</sub> Fe/N-C	4 h/cycle for 105 cycles; 420 h@10 mA cm <sup>-2</sup>	S52
NiO/Ni(OH) <sub>2</sub>	70 min/cycle for 70 cycles; 82 h@1 mA cm <sup>-2</sup>	S53
Fe@NC	600 s/cycle for 100 cycles; 17 h@10 mA cm <sup>-2</sup>	S54
BNC	600 s/cycle for 66 cycles; 11 h@20 mA cm <sup>-2</sup>	S55
c-CoMn <sub>2</sub> /C	400 s/cycle for 155 cycles; 17 h@10 mA cm <sup>-2</sup>	S56
CCBC-2	600 s/cycle for 75 cycles; 12.5 h@2 mA cm <sup>-2</sup>	S57
RuSn73	600 s/cycle for 100 cycles; 16.6 h@10 mA cm <sup>-2</sup>	S58
α-MnO <sub>2</sub> /CNT <sub>10</sub>	300 s/cycle for 100 cycles; 8.33 h@10 mA cm <sup>-2</sup>	S59

**Table S7.** Comparison of ionic conductivities of previously developed electrolytes.

Electrolyte	Ionic conductivity (S cm <sup>-1</sup> )	References
Functionalized Bio-cellulose	$6.4 \times 10^{-2}$	This work
Hydroxide-cellulose	$2.12 \times 10^{-2}$	S62
Li <sub>3.25</sub> Ge <sub>0.25</sub> P <sub>0.75</sub> S	$2.2 \times 10^{-3}$	S64
QPBI	$5.6 \times 10^{-2}$	S65
A201	$4.0 \times 10^{-2}$	S66
QAFCGO	$3.3 \times 10^{-2}$	S66
PVA/PDDA	$2.5 \times 10^{-2}$	S67
PPO-DMHDA	$3.5 \times 10^{-2}$	S68
AAEM	$3.2 \times 10^{-2}$	S69
Gelatin	$3.1 \times 10^{-3}$	S70
P(ECH-co-EO)	$1 \times 10^{-3}$	S71
PVA	$1.3 \times 10^{-4}$	S72
PVA-PVP	$2.6 \times 10^{-4}$	S73
PEO	$1 \times 10^{-3}$	S74

**Table S8.** Comparison of charge, ionic mobility, concentration and the transfer number of the cations and anions.

Ion	Charge valence ( $z_i$ )	Ionic mobility ( $\mu_i$ , m <sup>2</sup> s <sup>-1</sup> V <sup>-1</sup> )	Concentration ( $C_i$ , M)	Transfer number ( $t_i$ )
K <sup>+</sup>	1	$6.99 \times 10^{-8}$	6	0.245
Zn <sup>2+</sup>	2	$5.28 \times 10^{-8}$	0.2	0.0125
OH <sup>-</sup>	1	$2.06 \times 10^{-7}$	6	0.734
CH <sub>3</sub> COO <sup>-</sup>	1	$3.80 \times 10^{-8}$	0.4	0.009

**Table S9.** Summary of all-solid-state flexible rechargeable Zn–air batteries with various electrocatalysts and electrolytes.

Catalyst	Electrolyte	Power density (mW/cm <sup>2</sup> )	Recharge ability	Reference
Mn/Fe-HIB-MOF	Functionalized Bio-cellulose membrane	193	10 min/cycle for 3600 cycles; 600 h	This work
Co <sub>4</sub> N/CNW/CC	PVA gel	-	20 min/cycle for 36 cycles; 12 h	S13
Co-N,B-CSs	PVA gel	-	6 min/cycle for 230 cycles; 23 h	S17
S-C <sub>2</sub> NA	Functionalized Cellulose film	187	2 h/cycle for 230 cycles; 460 h	S18
S-C <sub>2</sub> NA	Functionalized Cellulose film	187	30 min/cycle for 900 cycles; 450 h	S18
CMO/S-300	PVA gel	-	30 min/cycle for 20 cycles; 10 h	S22
DN-CP@G	PVA gel	-	60 min/cycle for 170 cycles; 170 h	S24
NCNF-1000	PVA gel	-	10 min/cycle for 48 cycles; 8 h	S26
NC-Co <sub>3</sub> O <sub>4</sub> -90	Acrylic acid gel	82	24 min/cycle for 60 cycles; 24 h	S28
FeNi@N-GR	PVA gel	-	20 min/cycle for 54 cycles; 18 h	S29
N-GCNT/FeCO-3	PVA gel	97.8	10 min/cycle for 72 cycles; 12 h	S34
CNT@POF	PVA gel	-	4 min/cycle for 12 cycles; 48 min	S37
CuS/NiS <sub>2</sub>	PVA gel	-	10 min/cycle for 150 cycles; 25 h	S45
Co <sub>3</sub> O <sub>4</sub> -NCNT/SS	Cellulose film	-	20 min/cycle for 1500 cycles; 500 h	S60
MnO <sub>x</sub> -GCC	Acrylic acid gel	32	20 min/cycle for 175 cycles; 58 h	S61
Co <sub>3</sub> O <sub>4</sub>	Cellulose membrane	-	1 h/cycle for 35 cycles; 35 h	S62
LaNiO <sub>3</sub> /NCNT	PVA gel	-	20 min/cycle for 120 cycles; 40 h	S63

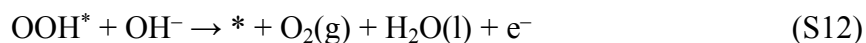
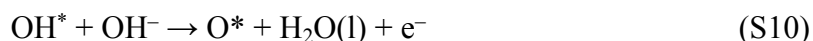
## 2. Theoretical Methods

### Computational Details and Modeling

All *ab initio* calculations were performed with the Vienna *Ab initio* Simulation Package (VASP 5.4.1).<sup>S75-S78</sup> We used the BEEF-vdW<sup>S79</sup> exchange-correlation functional using the projector augmented wave (PAW) method<sup>S80-S81</sup> with a generalized gradient to accurately describe the chemisorption as well as physisorption of metal–organic complex. Integration in the Brillouin zone was performed based on the Monkhorst-Pack scheme using a  $\Gamma$ -centered  $4 \times 4 \times 1$  (Fe-HIB-MOF),  $4 \times 4 \times 1$  (Mn-HIB-MOF), and  $3 \times 4 \times 1$  (Mn/Fe-HIB-MOF) k-point mesh in each primitive lattice vector of the reciprocal space for geometric optimization. A plane-wave cutoff energy of 500 eV was used. Lattice constants and internal atomic positions were fully optimized by the spin polarization calculation until the residual forces were less than 0.04 eV/Å. The schematics of our models are shown as Supplementary Fig. S43. For the convenience of identifying the active positions, we name them by element name and Arabic number. The details of the position site naming are also included in Supplementary Fig. S43.

### OER and ORR Reaction Pathways

In this work, we followed the theoretically well-defined approach proposed by Norskov group, which has been generally accepted method for the electrochemical activity studies. It is the theoretical approach previously developed for modeling the thermochemistry of electrochemical reactions based on density functional calculations in which the thermodynamic stabilities of the intermediates can be considered as the main indicator on the catalytic activity.<sup>S82,83</sup> The generally acceptable OER mechanism is the four electron associative mechanism.<sup>S84</sup> The four elementary steps are described as follows:



where \* represents the active site, and OH\*, O\*, and OOH\* are adsorbed intermediates. In the ORR reaction, we considered the overall reaction mechanism for the complete direct four-electron process in which O<sub>2</sub> is reduced to water without the formation of the hydrogen peroxide intermediate, H<sub>2</sub>O<sub>2</sub>. The ORR mechanism in an alkaline environment could occur in the following four electron reaction pathways,



Reactions (S13) to (S17) for ORR are the inversed forms of reactions (S9) to (S12) for OER.

### Derivation of the free energy relations

We calculated the reaction free energies of the intermediates O\*, OH\* and OOH\* on the Mn-HIB-MOF, Fe-HIB-MOF, and Mn/Fe-HIB-MOF to determine the point of the rate-limiting step of OER and ORR on various active sites for different structure. For each step, the reaction free energy  $\Delta G_{\text{ads}}$  is expressed by

$$\Delta G_{\text{ads}} = \Delta E^{\text{ads}} + \Delta \text{ZPE} - T\Delta S \quad (\text{S18})$$

where ZPE is the zero-point energy, T is the temperature, and  $\Delta S$  is the entropy change. The correction terms are listed in supplementary Table S10–S11. Subsequently, we constructed free energy diagrams (FED) considering the following four electron reaction paths with equations at standard conditions.<sup>S84</sup>

The free energy change of each elementary reaction of OER in alkaline media can be expressed as follows:

$$\Delta G_1 = G_{\text{OH}^*} + \mu_{\text{e}^-} - (\mu_{\text{OH}^-} + G_*) \quad (\text{S19})$$

$$\Delta G_2 = G_{O^*} + \mu_{H_2O(l)} + \mu_{e^-} - (G_{OH^*} + G^*) \quad (S20)$$

$$\Delta G_3 = G_{OOH^*} + \mu_{e^-} - (G_{O^*} + \mu_{OH^-}) \quad (S21)$$

$$\Delta G_4 = G^* + \mu_{O_2} + \mu_{H_2O(l)} + \mu_{e^-} - (G_{OOH^*} + \mu_{OH^-}) \quad (S22)$$

The free energy change of each elementary reaction can be calculated using the chemical potentials of hydroxide, electron, liquid water, and oxygen molecule ( $\mu_{OH^-}$ ,  $\mu_{e^-}$ ,  $\mu_{H_2O(l)}$  and  $\mu_{O_2}$ ) and the free energies of each intermediate ( $G_{OH^*}$ ,  $G_{O^*}$ , and  $G_{OOH^*}$ ) on the surface of catalyst (\*). Moreover, the free energy relations of the ORR in alkaline media can also be explained in the same way as the OER mentioned above.

### Free energy diagram (FED) and Overpotential ( $\eta$ )

We can deduce an important parameter of electrocatalytic activity from the calculated  $\Delta G$ : the magnitude of the potential-determining step ( $G^{OER/ORR}$ ) in consecutive reaction steps. This is the specific reaction step with the largest  $\Delta G$  in the OER and ORR elementary reaction steps; i.e., the concluding step to achieve a downhill reaction in the free energy diagram (FED) with increasing potential (Figure 8 and supplementary Figure S45):

$$G^{OER/ORR} = \max[\Delta G_1, \Delta G_2, \Delta G_3, \Delta G_4]^0 \quad (S23)$$

The theoretical overpotential at standard conditions is then given by (S23) in alkaline condition:

$$\eta^{OER/ORR} = (G^{OER/ORR}/e) - xV, \quad x = 0.402 \text{ V} \quad (S24)$$

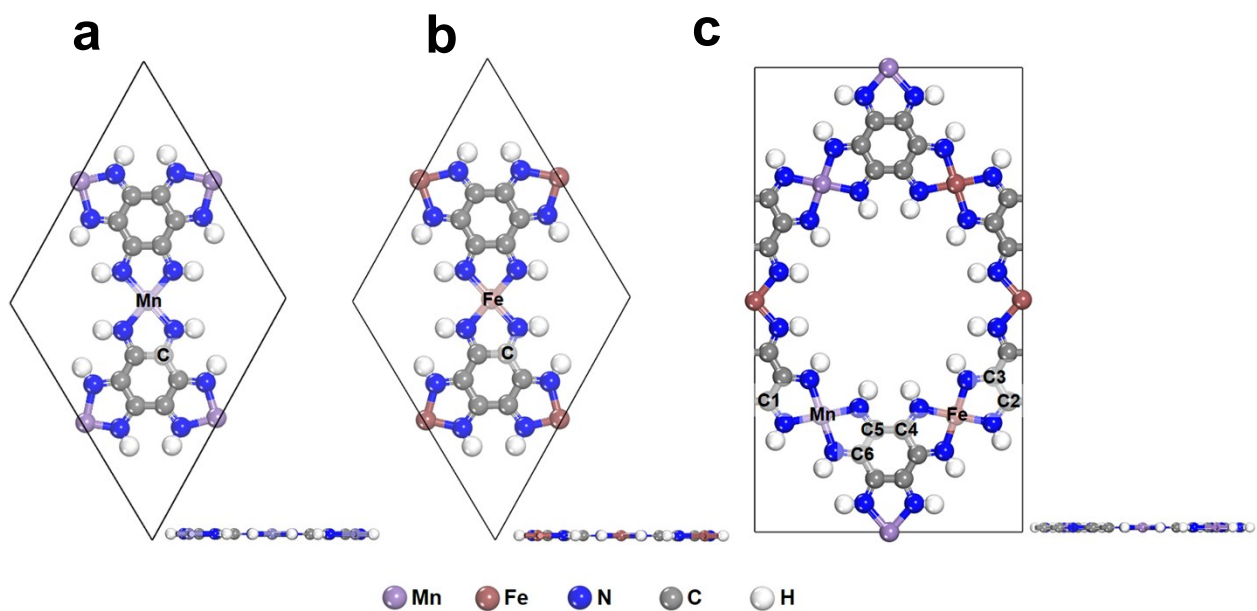


**Figure S43.** Structure of (a) Mn-HIB-MOF, (b) Fe-HIB-MOF and (c) Mn/Fe-HIB-MOF. (Inset: The active sites with elements and element numbers.)

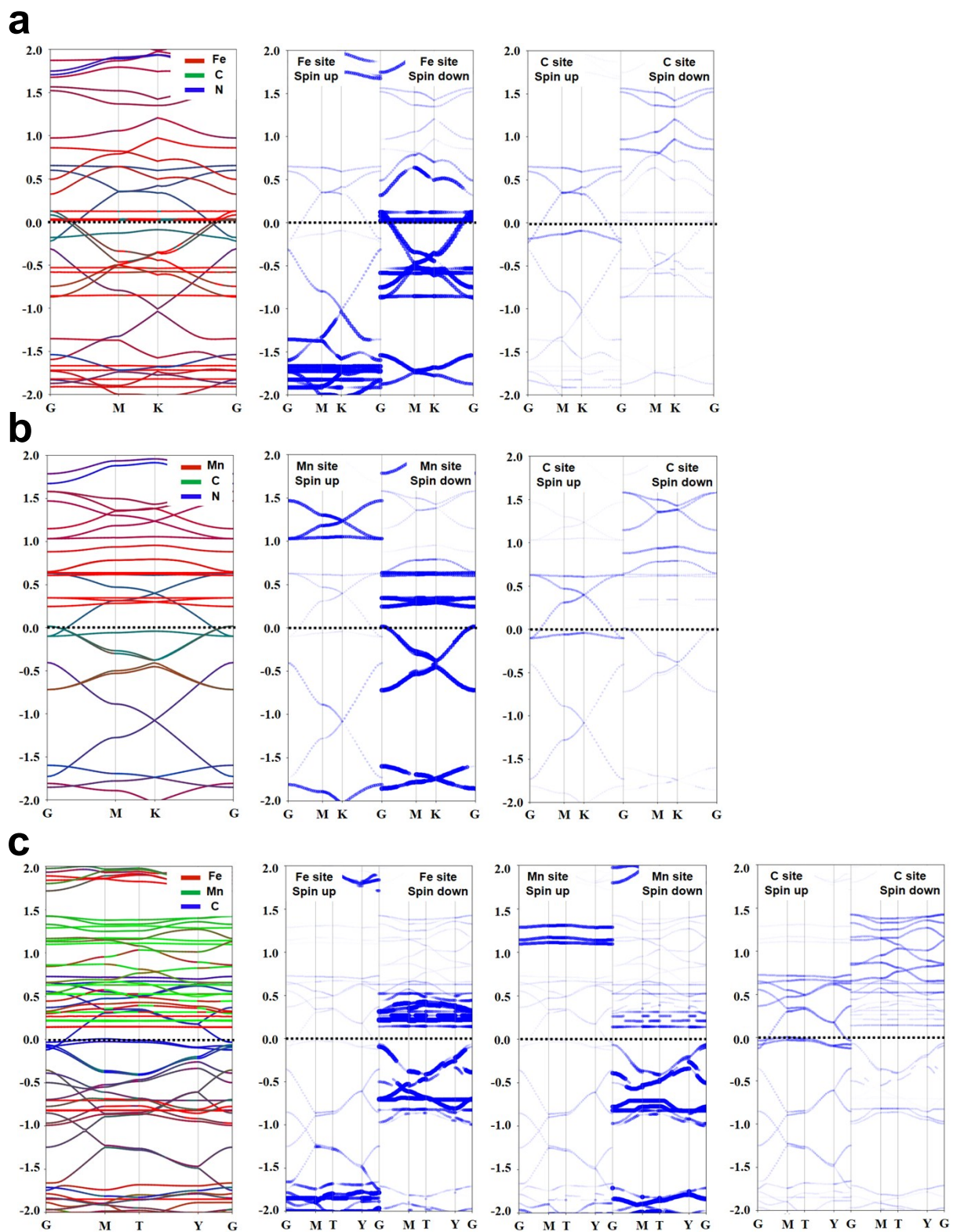


**Figure S44.** Band structures of (a) Fe-HIB-MOF, (b) Mn-HIB-MOF, and (c) Mn/Fe-HIB-MOF. The element-resolved band structure is also indicated by blue lines, and the Fermi energy is set to zero. It is focused on the Fe, Mn, or C site because these are the active sites for OER and ORR.

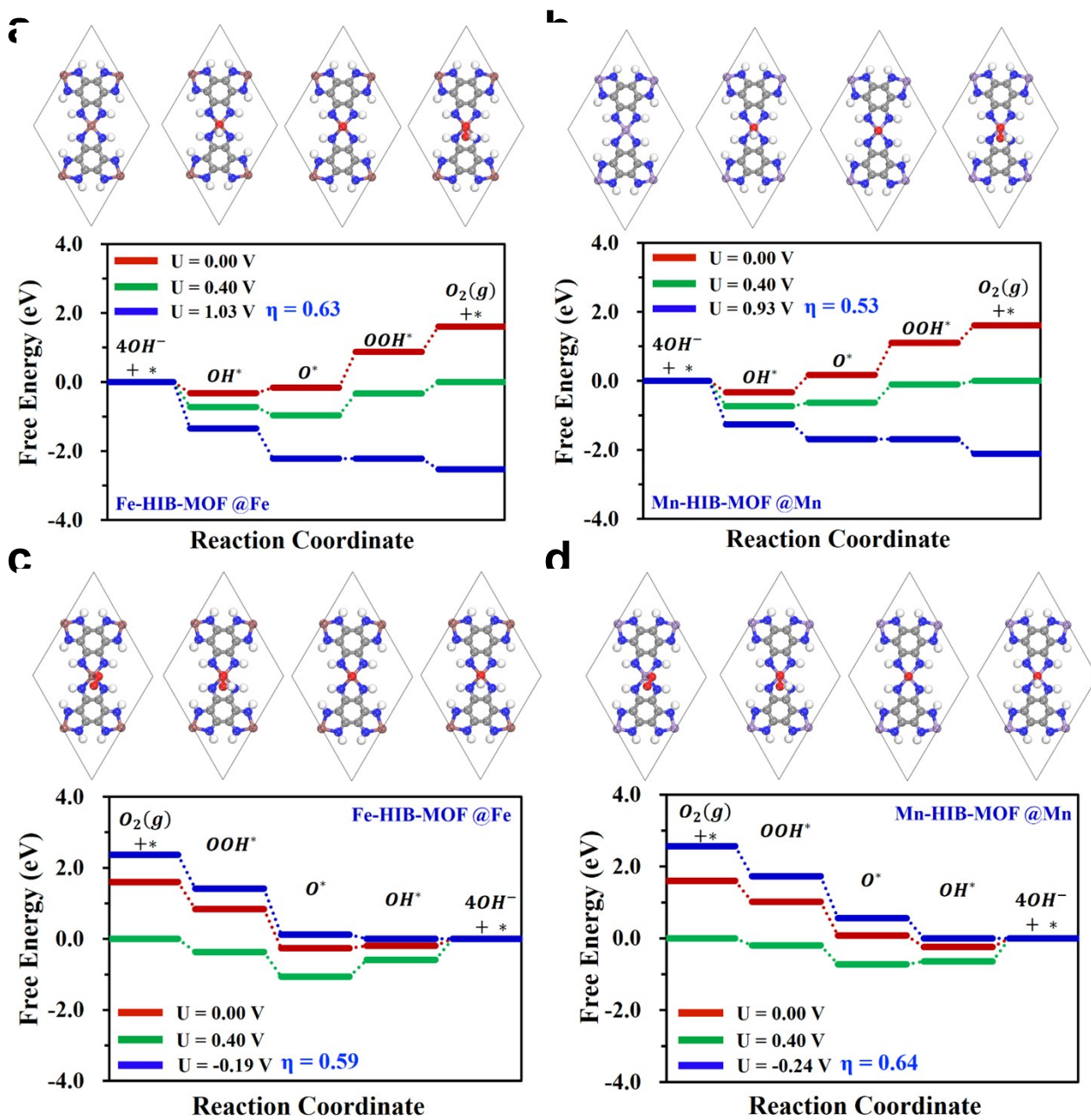


**Figure S45.** Free energy diagrams of Fe-HIB-MOF and Mn-HIB-MOF for the (a,b) OER and (c,d) ORR pathway.

Unlike the case of C, Fe or Mn active sites as shown in supplementary figure S45, the intermediate species adsorbed on N site can be easily transferred to the immediately adjacent Fe or Mn sites. Because these metal sites have the higher contribution to the frontier bands around the Fermi level, which strongly stabilize the intermediate species as shown in supplementary figure S44. The presence of hydrogen atoms adsorbed on nitrogen sites hinders stable binding configurations in the free space of abundant holes in M-HIB-MOFs, as shown in supplementary figure S43.

**Table S10.** Total energies (E) of H<sub>2</sub>O and H<sub>2</sub> and zero-point energy (ZPE) corrections and entropic contributions (TS) to the free energies.

Species	E (eV)	ZPE (eV)	TS (eV)
H <sub>2</sub> O (0.035 bar)	-14.70	0.56	0.67
H <sub>2</sub>	-7.47	0.27	0.41
O*	-	0.19	0.05
OH*	-	0.34	0.07
OOH*	-	0.42	0.16

**Table S11.** Frequencies of adsorbed species.

Adsorbed Species	Frequency (cm <sup>-1</sup> )
O*	2063.42, 587.47, 453.08
OH*	3742.38, 796.97, 439.35, 255.15, 68.51, 95.56
OOH*	3706.96, 1263.43, 719.66, 364.46, 177.46, 138.58, 170.03, 132.96, 138.25

**Table S12.** Reaction free energies for four-step four-electron reaction pathway for OER in alkaline media on different active sites.

Four step four-electron OER mechanism						
		$\text{OH}^- + * \rightarrow \text{OH}^* + \text{e}^-$				$(\Delta G_1)$
		$\text{OH}^* + \text{OH}^- \rightarrow \text{O}^* + \text{H}_2\text{O}(\text{l}) + \text{e}^-$				$(\Delta G_2)$
		$\text{O}^* + \text{OH}^- \rightarrow \text{OOH}^* + \text{e}^-$				$(\Delta G_3)$
		$\text{OOH}^* + \text{OH}^- \rightarrow * + \text{O}_2(\text{g}) + \text{H}_2\text{O}(\text{l}) + \text{e}^-$				$(\Delta G_4)$
Material	Active site	$\Delta G_1$	$\Delta G_2$	$\Delta G_3$	$\Delta G_4$	$\eta^{\text{OER}}$
Fe-HIB-MOF	Fe	-0.38	0.16	1.03	0.80	0.63
	C	0.43	0.36	1.06	-0.25	0.66
Mn-HIB-MOF	Mn	-0.33	0.51	0.93	0.50	0.53
	C	0.60	0.29	0.96	-0.23	0.56
Mn/Fe-HIB-MOF	Fe	-0.74	0.63	0.83	0.89	0.43
	Mn	-0.78	0.05	1.40	0.93	1.00
	C1	0.37	0.32	1.00	-0.08	0.60
	C2	0.39	0.51	0.86	-0.15	0.46
	C3	0.44	0.46	0.85	-0.14	0.45
	C4	0.37	0.53	0.77	-0.06	0.37
	C5	0.32	0.50	0.88	-0.08	0.47
C6	0.29	0.52	0.85	-0.06	0.45	

**Table S13.** Reaction free energies for four-step four-electron reaction pathway for ORR in alkaline media on different active sites. We include the O<sub>2</sub> adsorption free energy ( $\Delta G_{O_2^*}$ ) in FED with  $\Delta G_1 = \Delta G_{O_2^*} + \Delta G_1'$ .

Four step four-electron ORR mechanism								
		$O_2(g) + * \rightarrow O_2^*$						$(\Delta G_{O_2^*})$
		$O_2^* + H_2O(l) + e^- \rightarrow OOH^* + OH^-$						$(\Delta G_1')$
		$OOH^* + e^- \rightarrow O^* + OH^-$						$(\Delta G_2)$
		$O^* + H_2O(l) + e^- \rightarrow OH^* + OH^-$						$(\Delta G_3)$
		$OH^* + e^- \rightarrow * + OH^-$						$(\Delta G_4)$
Material	Active site	$\Delta G_{O_2^*}$	$\Delta G_1'$	$\Delta G_1$	$\Delta G_2$	$\Delta G_3$	$\Delta G_4$	$\eta^{ORR}$
Fe-HIB-MOF	Fe	-1.14	0.38	-0.76	-1.10	0.07	0.19	0.59
	C	-0.64	0.80	0.16	-1.07	-0.14	-0.56	0.56
Mn-HIB-MOF	Mn	-0.74	0.15	-0.59	-0.94	-0.32	0.24	0.64
	C	-0.52	0.77	0.21	-1.04	-0.06	-0.72	0.65
Mn/Fe-HIB-MOF	Fe	-1.04	0.11	-0.92	-0.90	-0.40	0.61	1.02
	Mn	-0.93	-0.03	-0.96	-1.47	0.18	0.65	1.06
	C1	-0.29	0.34	0.05	-1.07	-0.09	-0.49	0.45
	C2	-0.63	0.74	0.11	-0.93	-0.28	-0.51	0.52
	C3	-0.62	0.73	0.11	-0.92	-0.23	-0.57	0.51
	C4	-0.63	0.65	0.02	-0.84	-0.30	-0.50	0.43
	C5	-0.61	0.66	0.05	-0.95	-0.27	-0.44	0.45
C6	-0.63	0.66	0.02	-0.92	-0.29	-0.42	0.43	

## Supplementary Videos

**Video S1.** Practical demonstration for powering RED, GREEN, and BLUE LEDs connected in parallel (RED, BLUE, and GREEN) by using three solid-state ZABs with Mn/Fe-HIB-MOF as the air cathode and FBN membrane as the electrolyte (under switching ON and OFF conditions).

The video shows (i) an assembled configuration of three solid-state ZABs connected in series with Mn/Fe-HIB-MOFs as air electrode and red, green, and blue LEDs; (ii) the high open-circuit voltage of  $\sim 4.25$  V powering these LEDs simultaneously; (iii) the ON/OFF switching prospects for all LEDs, illustrating outstanding performance of these ZABs.

**Video S2.** Commercial SAMSUNG Galaxy smartphone charging demonstration by using three solid-state ZABs with Mn/Fe-HIB-MOF as the air cathode and FBN membrane as the electrolyte.

The video displays (i) an assembled configuration of three solid-state ZABs connected in series with Mn/Fe-HIB-MOFs as air electrode and FBN electrolyte and (ii) live demonstration of charging SAMSUNG Galaxy smartphone, illustrating the probability for commercialization of fabricated ZABs.

## Supplementary References

- (S1) Liang, Y.; Wang, H.; Zhou, J.; Li, Y.; Wang, J.; Regier, T.; Dai, H. *J. Am. Chem. Soc.* 2012, 134, 3517–3523.
- (S2) U. Paulus, T. Schmidt, and H. Gasteiger, R. Behm, *J. Electroanal. Chem.* 2001, 495, 134.
- (S3) Zecevic, S.; Wainright, J.; Litt, M.; Gojkovic, S.; Savinell, R. *J. Electrochem. Soc.* 1997, 144, 2973–2982.
- (S4) Antoine, O.; Durand, R. *J. Appl. Electrochem.* 2000, 30, 839–844.
- (S5) J. Dou, L. Sun, Y. Ge, W. Li, C. Hendon, J. Li, S. Gul, J. Yano, E. Stach, M. Dincă, *J. Am. Chem. Soc.* 2017, 139, 13608–13611.
- (S6) D. Feng, T. Lei, M. R. Lukatskaya, J. Park, Z. Huang, M. Lee, L. Shaw, S. Chen, A. Yakovenko, A. Kulkarni, J. Xiao, K. Fredrickson, J. Tok, X. Zou, Y. Cui, Z. Bao, *Nat. Energy* 2018, 3, 30-36.
- (S7) Ou, J.; Zhang, Y.; Chen, L.; Zhao, Q.; Meng, Y.; Guo, Y.; Xiao, D. *J. Mater. Chem. A* 2015, 3, 6534–6541.
- (S8) Wang, Y.; Bai, X.; Pan, C.; He J.; Zhu, Y. *J. Mater. Chem.* 2012, 22, 11568–11573.
- (S9) Cui, Y.; Zhang, J.; Zhang, G.; Huang, J.; Liu, P.; Antonietti, M.; Wang, X. *J. Mater. Chem.* 2011, 21, 13032–13039.
- (S10) Zhang, J.; Zhao, Z.; Xia, Z.; Dai, L. *Nat. Nanotechnol.* 2015, 10, 444-452.
- (S11) Yin, J.; Li, Y.; Lv, F.; Fan, Q.; Zhao, Y.; Zhang, Q.; Wang, W.; Cheng, F.; Xi, P.; Guo, S. *ACS Nano* 2017, 11, 2275–2283.
- (S12) Shinde, S.; Lee, C.; Sami, A.; Kim, D.; Lee, S.; Lee, J. *ACS Nano* 2017, 11, 347–357.
- (S13) Meng, F.; Zhong, H.; Bao, D.; Yan, J.; Zhang X. *J. Am. Chem. Soc.* 2016, 138, 10226–10231.
- (S14) Wang, X.; Li, Y.; Jin, T.; Meng, J.; Jiao, L.; Zhu, M.; Chen, J. *Nano Lett.* 2017, 17, 7989–7994.
- (S15) Pei, Z.; Li, H.; Huang, Y.; Xue, Q.; Huang, Y.; Zhu, M.; Wang, Z.; Zhi, C. *Energy Environ. Sci.* 2017, 10, 742-749.
- (S16) Zhang, M.; Dai, Q.; Zheng, H.; Chen, M.; Dai, L. *Adv. Mater.* 2018, 30, 1705431.
- (S17) Guo, Y.; Yuan, P.; Zhang, J.; Hu, Y.; Amiin, I.; Wang, X.; Zhou, J.; Xia, H.; Song, Z.; Xu, Q.; Mu, S. *ACS Nano* 2018, 12, 1894–1901.
- (S18) Shinde, S.; Lee, C.; Yu, J.; Kim, D.; Lee, S.; Lee, J. *ACS Nano* 2018, 12, 596–608.

- (S19) Ma, L.; Chen, S.; Pei, Z.; Huang, Y.; Liang, G.; Mo, F.; Yang, Q.; Su, J.; Gao, Y.; Zapien, J.; Zhi, C. *ACS Nano* 2018, 12, 1949–1958.
- (S20) Kashyap, V.; Kurungot, S. *ACS Catal.* 2018, 8, 3715–3726.
- (S21) Wang, Q.; Ji, Y.; Lei, Y.; Wang, Y.; Wang, Y.; Li, Y.; Wang, S. *ACS Energy Lett.* 2018, 3, 1183–1191.
- (S22) Peng, S.; Han, X.; Li, L.; Chou, S.; Ji, D.; Huang, H.; Du, Y.; Liu, J.; Ramakrishna, S. *Adv. Energy Mater.* 2018, 8, 1800612.
- (S23) Jiang, Y.; Deng, Y.; Fu, J.; Lee, D.; Liang, R.; Cano, Z.; Liu, Y.; Bai, Z.; Hwang, S.; Yang, L.; Su, D.; Chu, W.; Chen, Z. *Adv. Energy Mater.* 2018, 8, 1702900.
- (S24) Hang, C.; Zhang, J.; Zhu, J.; Li, W.; Kou, Z.; Huang, Y. *Adv. Energy Mater.* 2018, 8, 1703539.
- (S25) Yang, H.; Miao, J.; Hung, S.; Chen, J.; Tao, H.; Wang, X.; Zhang, L.; Chen, R.; Gao, J.; Chen, H.; Dai, L.; Liu, B. *Sci. Adv.* 2016, 2, e1501122.
- (S26) Liu, Q.; Wang, Y.; Dai, L.; Yao, J. *Adv. Mater.* 2016, 28, 3000–3006.
- (S27) Han, X.; Wu, X.; Zhong, C.; Deng, Y.; Zhao, N.; Hu, W. *Nano Energy* 2017, 31, 541–550.
- (S28) Guan, C.; Sumboja, A.; Wu, H.; Ren, W.; Liu, X.; Zhang, H.; Liu, Z.; Cheng, C.; Pennycook, S.; Wang, J. *Adv. Mater.* 2017, 29, 1704117.
- (S29) Liu, P.; Gao, D.; Xiao, W.; Ma, L.; Sun, K.; Xi, P.; Xue, D.; Wang, J. *Adv. Funct. Mater.* 2018, 28, 1706928.
- (S30) Shinde, S.; Yu, J.; Song, J.; Nam, Y.; Kim, D.; Lee, J. *Nanoscale Horiz.* 2017, 2, 333–341.
- (S31) Chen, P.; Zhou, T.; Xing, L.; Xu, K.; Tong, Y.; Xie, H.; Zhang, L.; Yan, W.; Chu, W.; Wu, C.; Xie, Y. *Angew. Chem., Int. Ed.* 2017, 56, 610–614.
- (S32) Li, G.; Wang, X.; Fu, J.; Li, J.; Park, M.; Zhang, Y.; Lui, G.; Chen, Z. *Angew. Chem., Int. Ed.* 2016, 55, 4977–4982.
- (S33) Ma, T.; Ran, J.; Dai, S.; Jaroniec, M.; Qiao, S. *Angew. Chem., Int. Ed.* 2015, 54, 4646–4650.
- (S34) Su, C.; Cheng, H.; Li, W.; Liu, Z.; Li, N.; Hou, Z.; Bai, F.; Zhang, H.; Ma, T. *Adv. Energy Mater.* 2017, 7, 1602420.
- (S35) Mao, S.; Wen, Z.; Huang, T.; Hou, Y.; Chen, J. *Energy Environ. Sci.* 2014, 7, 609–616.
- (S36) Liu, W.; Zhang, J.; Bai, Z.; Jiang, G.; Li, M.; Feng, K.; Yang, L.; Ding, Y.; Yu, T.; Chen, Z.; Yu, A. *Adv. Funct. Mater.* 2018, 28, 1706675.

- (S37) Li, B.; Zhang, S.; Wang, B.; Xia, Z.; Tang, C.; Zhang, Q. *Energy Environ. Sci.* 2018, 11, 1723-1729.
- (S38) Yang, T.; Venkatesan, S.; Lien, C.; Chang, J.; Zen, J. *Electrochim. Acta*, 2011, 56, 6205–6210.
- (S39) Liu, Y.; Chen, S.; Quan, X.; Yu, H.; Zhao, H.; Zhang, Y.; Chen, G. *J. Phys. Chem. C* 2013, 117, 14992–14998.
- (S40) Prabu, M.; Ketpang, K.; Shanmugam, S. *Nanoscale*, 2014, 6, 3173–3181.
- (S41) Cao, R.; Thapa, R.; Kim, H.; Xu, X.; Kim, M.; Li, Q.; Park, N.; Liu, M.; Cho, J. *Nat. Commun.* 2013, 4, 2076.
- (S42) Li, Y.; Gong, M.; Liang, Y.; Feng, J.; Kim, J.; Wang, H.; Hong, G.; Zhang, B.; Dai, H. *Nat. Commun.* 2013, 4, 1805.
- (S43) Dhavale, V.; Kurungot, S. *ACS Catal.* 2015, 5, 1445–1452.
- (S44) Lee, J.; Park, G.; Lee, H.; Kim, S.; Cao, R.; Liu, M.; Cho, J. *Nano Lett.* 2011, 11, 5362–5366.
- (S45) An, L.; Li, Y.; Luo, M.; Yin, J.; Zhao, Y.; Xu, C.; Cheng, F.; Yang, Y.; Xi, P.; Guo, S. *Adv. Funct. Mater.* 2017, 27, 1703779.
- (S46) Li, L.; Liu, C.; He, G.; Fan, D.; Manthiram, A. *Energy Environ. Sci.* 2015, 8, 3274–3282.
- (S47) Lee, D.; Choi, J.; Feng, K.; Park, H.; Chen, Z. *Adv. Energy Mater.* 2014, 4, 1301389.
- (S48) Liu, X.; Park, M.; Kim, M.; Gupta, S.; Wu, G.; Cho, J. *Angew. Chem., Int. Ed.* 2015, 54, 9654–9658.
- (S49) Jung, J.; Risch, M.; Park, S.; Kim, M.; Nam, G.; Jeong, H.; Horn, Y.; Cho, J. *Energy Environ. Sci.* 2016, 9, 176–183.
- (S50) Wang, T.; Nam, G.; Jin, Y.; Wang, X.; Ren, P.; Kim, M.; Liang, J.; Wen, X.; Jang, H.; Han, J.; Huang, Y.; Li, Q.; Cho, J. *Adv. Mater.* 2018, 30, 1800757.
- (S51) Fu, G.; Chen, Y.; Cui, Z.; Li, Y.; Zhou, W.; Xin, S.; Tang, Y.; Goodenough, J. *Nano Lett.* 2016, 16, 6516–6522.
- (S52) Fu, G.; Cui, Z.; Chen, Y.; Li, Y.; Tang, Y.; Goodenough, J. *Adv. Energy Mater.* 2017, 7, 1601172.
- (S53) Lee, D.; Fu, J.; Park, M.; Liu, H.; Kashkooli, A.; Chen, Z. *Nano Lett.* 2016, 16, 1794–1802.
- (S54) Wang, J.; Wu, H.; Gao, D.; Miao, S.; Wang, G.; Bao, X. *Nano Energy* 2015, 13, 387–396.

- (S55) Zhuang, X.; Gehrig, D.; Forler, N.; Liang, H.; Wagner, M.; Hansen, M.; Laquai, F.; Zhang, F.; Feng, X. *Adv. Mater.* 2015, 27, 3789–3796.
- (S56) Li, C.; Han, X.; Cheng, F.; Hu, Y.; Chen, C.; Chen, J. *Nat. Commun.* 2015, 6, 7345.
- (S57) Chen, Z.; Yu, A.; Higgins, D.; Li, H.; Wang, H.; Chen, Z. *Nano Lett.* 2012, 12, 1946–1952.
- (S58) T. You and C. Hu, *ACS Appl. Mater. Interfaces* 2018, 10, 10064–10075.
- (S59) P. Li, C. Hu, T. You, P. Chen, *Carbon*, 2017, 111, 813-821.
- (S60) Fu, J.; Hassan, F.; Li, J.; Lee, D.; Ghannoum, A.; Lui, G.; Hoque, M.; Chen, Z. *Adv. Mater.* 2016, 28, 6421–6428.
- (S61) Sumboja, A.; Lübke, M.; Wang, Y.; An, T.; Zong, Y.; Liu, Z. *Adv. Energy Mater.* 2017, 7, 1700927.
- (S62) Fu, J.; Zhang, J.; Song, X.; Zarrin, H.; Tian, X.; Qiao, J.; Rasen, L.; Lib, K.; Chen, Z. *Energy Environ. Sci.* 2016, 9, 663–670.
- (S63) Fu, J.; Lee, D.; Hassan, F.; Yang, L.; Bai, Z.; Park, M.; Chen, Z. *Adv. Mater.* 2015, 27, 5617–5622.
- (S64) Y. Li, X. Wang, S. Dong, X. Chen, G. Cui, *Adv. Energy Mater.* 2016, 6, 1600751.
- (S65) Z. Xia, S. Yuan, G. Jiang, X. Guo, J. Fang, L. Liu, J. Qiao, J. Yin, *J. Membrane Sci.* 2012, 390–391, 152.
- (S66) J. Zhang, J. Fu, X. Song, G. Jiang, H. Zarrin, P. Xu, K. Li, A. Yu, Z. Chen, *Adv. Energy Mater.* 2016, 6, 1600476.
- (S67) J. Qiao, J. Zhang, J. Zhang, *J. Power Sources*, 2013, 237, 1.
- (S68) N. Li, T. Yan, Z. Li, T. Thurn Albrecht, W. Binder, *Energy Environ. Sci.* 2012, 5, 7888.
- (S69) J. Ran, L. Wu, J. Varcoe, A. Ong, S. Poynton, T. Xu, *J. Membrane Sci.* 2012, 415–416, 242.
- (S70) J. Park, M. Park, G. Nam, J. Lee, J. Cho, *Adv. Mater.* 2015, 27, 1396.
- (S71) N. Vassal, E. Salmon, J. Fauvarque, *Electrochim. Acta* 2000, 45, 1527.
- (S72) A. Lewandowski, K. Skorupska, J. Malinska, *Solid State Ionics* 2000, 133, 265.
- (S73) F. Hatta, M. Yahya, A. Ali, R. Subban, M. Harun, A. Mohamad, *Ionics* 2005, 11, 418.
- (S74) J. Fauvarque, S. Guinot, N. Bouzir, E. Salmon, J. Penneau, *Electrochim. Acta* 1995, 40, 2449.
- (S75) G. Kresse, J. Hafner, *Phys. Rev. B.* 1993, 48, 13115-13118.

- (S76) G. Kresse, J. Hafner, Phys. Rev. B. 1994, 49, 14251-14269.
- (S77) G. Kresse, J. Furthmuller, Comp. Mater. Sci. 1996, 6, 15-50.
- (S78) G. Kresse, J. Furthmuller, Phys. Rev. B. 1996, 54, 11169-11186.
- (S79) J. Wellendorff, K. Lundgaard, A. Mogelhoj, V. Petzold, D. Landis, J. Norskov, T. Bligaard, K. Jacobsen, Phys. Rev. B. 2012, 85, 235149.
- (S80) G. Kresse, D. Joubert, Phys. Rev. B. 1999, 59, 1758-1775.
- (S81) P. E. Blochl, Phys. Rev. B. 1994, 50, 17953-17979.
- (S82) J. Rossmeisl, Z-W. Qu, H. Zhu, G-J. Kroes, J.K. Norskov, J. Electroanal. Chem. 2007, 607, 83.
- (S83) J. K. Norskov, J. Rosmeisl, A. Logadottir and L. Lindqvist, *J. Phys. Chem. B.* 2004, 108, 17886.
- (S84) I. Man, H. Su, F. Calle-Vallejo, H. Hansen, J. Martinez, N. Inoglu, J. Kitchin, T. Jaramillo, J. Norskov, J. Rossmeisl, Chemcatchem. 2011, 3, 1159-1165.